Three dimensional spiral injection scheme for g-2/EDM experiment at J-PARC

Hiromi Iinuma*, Hisayoshi Nakayama, Katsunobu Oide, Kennichi Sasaki, Naohito Saito, Tsutomu Mibe

KEK, Oho 1-1, Tsukuba, Japan

Mitsushi Abe

Hitachi, Japan

Gerry Bunce

Colorado, the U.S.

Abstract

Three dimensional spiral injection scheme is an one of major R&D items for the newly planned muon $g-2$/EDM experiment at J-PARC. The new experiment aims factor three better precision of $g-2$ and 100 times better sensitivity of EDM measurements compared to the previous experiments. We take advantage of 3-T MRI solenoid magnet as the muon storage with 0.66 m diameter, to achieve 1 ppm level of local uniformity. There is no previous instance to inject accelerated beam into such a small ring. Conventional injection scheme is not applicable because of several technical difficulties. New injection scheme solves these difficulties and provide smooth beam injection utilizing a static solenoidal fringe field of the storage magnet. The strongest point of this scheme is the following: it does not cause any error field in the storage volume in principle. But, there is a challenging issue: the beam requires strong coupling horizontally and vertically. To accomplish the higher injection effiency, this is an indispensable item. In this document, we introduce basic kinetics of spiral motion of the

☆Detail information of the new $g-2$/EDM experiment at J-PARC is available in the homepage on $g-2$/EDM.

*Corresponding author

Email address: iinuma.hiromi@kek.jp (Hiromi Iinuma)

beam in the solenoid fringe field, and a required phase-space at the entrance of the storage magnet (injection point). We discuss Transfer Matrix of beam transport line which applies proper strong coupling. Stable and precise beam control at the storage volume connects to the sensitivity of EDM directly. We introduce a concept and realistic design of the beam storage system: the Weak focusing and vertical kicker system.

Keywords: `new beam injection scheme`, $g-2$/EDM, J-PARC

1. Introduction

The new experiment of the muon's anomalous magnetic moment $(g-2)$ and its electric dipole moment (EDM) is in preparation at J-PARC muon facility at MLF, MUSE. The principle of the experiment is the same as for the former experiments at CERN and BNL. The differences two angular frequencies between the spin precession frequency ω_s and the orbital cyclotron precession frequency ω_c is measured in a homogeneous magnetic field and hence $(g-2)$ is determined.

On the other hand, the J-PARC muon $g-2$/EDM measurement will use a very different approach to previous muon $g-2$ experiments. Table 1 compares the proposed experiment with the previous experiment, BNL-E821[1, 2]. Firstly we review experimental parameters in previous experiment.

Previous experiments used 3.09 GeV/c muons and a 14 m diameter storage ring, and used calorimetry to measure the decay positrons. The energy of the previous experiments was set by a cancellation in the contribution to the spin precession from from strong electric focusing at this energy.

For J-PARC, it is proposed to develop a source of ultra-cold muons[3, 4], which require only weak focusing to maintain in the beam size in a storage ring. This release the requirement on the muon energy, and a momentum of 300 MeV/c was chosen with a 3 T MRI-type solenoid magnet used to store the muons. In this case, the diameter of the orbital cyclotron motion becomes only 0.66 m. The J-PARC experiment will use an order of magnitude lower energy and twenty times smaller diameter storage ring. We expect to achieve the

Table 1: Comparison of the previous experiment BNL-E821 (its continuation at Fermilab, FNAL-E989) and this experiment.Arrows in the right column mean ultimate goal.

	BNL-E821	FNAL-E989	This Experiment
Muon momentum	3.09 GeV/c		0.3 GeV/c
γ	29.3		3
Polarization	100%		50%→ 100%
Storage field	$B = 1.45$ T		$B = 3.0$ T
Diameter of the ring	14 m		0.66 m
Focusing field	Electric Quad.		very-weak magnetic
Cyclotron period	149 ns		7.4 ns
Spin precession period	4.37 μs		2.11 μs
# of detected e^+	5.0×10^9	1.8×10^{11}	$8.7 \times 10^{11} \rightarrow 1.5 \times 10^{12}$
# of detected e^-	3.6×10^9	–	–
Statistical precision (a_μ)	0.46 ppm	0.14 ppm	0.37 ppm → 0.14 ppm
Statistical precision (EDM)	0.9×10^{-19} $e \cdot$ cm	10^{-21} $e \cdot$ cm	10^{-21} $e \cdot$ cm

better adjustment accuracy of the magnetic field with the smaller storage ring. Moreover, fiducial volume to detect decay positron (e^+) also compact. This fiducial volume is also inside of the well adjusted magnetic field. Therefore, we can track its trajectory and measure momentum event-by-event. This is the strongest point of the J-PARC muon $g-2$/EDM experiment. Because this system allow us to measure spin precession as an angular momentum vector. In case of non-zero electric dipole moment of the muon, as we introduce later, we can access to both $g-2$ and EDM signals at a time, with the same experimental set-up, by having an appropriate detector design.

Previous experiments reached a sensitivity on muon $g-2$ of 0.54 ppm, with the uncertainty dominated by statistics. The result, with most recent and sensitive from E821 at BNL, is not described by the Standard Model of particle physics, with a ~ 3 sigma deviation, suggesting the need for physics beyond the Standard Model. Muon $g-2$ is a fundamental observable of elementary particle

and it is valuable to improve upon its measurement and so to perform the experiment using different approaches. Any comprehensive theory of particle physics must describe muon $g-2$.

We will introduce two angular momentum vectors due to $g-2$ and EDM bellow. We also give an idea how precisely the muon beam should be controlled in the storage volume to detect EDM signal in order of 10^{-21} e·cm, which is 100 times better sensitivity compared to the previous experiment [2].

$g-2$ term. For a non-relativistic spin, the Hamiltonian is

$$H = -\vec{\mu}_\mu \cdot \vec{B} = -\frac{gq}{2m_\mu c}\vec{s}\cdot\vec{B}, \tag{1}$$

Here, $\vec{\mu}_\mu$ and m_μ are magnetic moment and mass of the muon respectively. g is a gyromagnetic ratio of the muon. c and q are the speed of light and an unit charge. The spin precession equation becomes

$$\frac{\mathrm{d}\vec{s}}{\mathrm{d}t} = \vec{\mu}_\mu \times \vec{B} = -\frac{gq}{2m_\mu c}\vec{B}\times\vec{s}. \tag{2}$$

and $|\vec{\omega}_L|$ is the Lamor frequency:

$$\vec{\omega}_L = \frac{gq}{2m_\mu c}\vec{B}. \tag{3}$$

Consider the muon moving with relativistic velocity $\vec{V}$ under the action of laboratory frame electric and magnetic fields: $\vec{B},\ \vec{E}$, respectively. Trajectory of the muon determined by the Lorentz force equation, with $\beta = \vec{V}/c$:

$$\frac{\mathrm{d}\vec{p}}{\mathrm{d}t} = q\left(\vec{E} + \vec{\beta}\times\vec{B}\right). \tag{4}$$

We can rewrite this equation as:

$$\frac{\mathrm{d}\vec{\beta}}{\mathrm{d}t} = \frac{q}{m_\mu c\gamma_\mu}\left[\vec{E} - \left(\vec{E}\cdot\vec{\beta}\right)\vec{\beta} + \vec{\beta}\times\vec{B}\right]. \tag{5}$$

The muon moving case, Equation 2 becomes:

$$\frac{\mathrm{d}\vec{s}}{\mathrm{d}t} = \vec{\omega_s}\times\vec{s}, \tag{6}$$

here,

$$\vec{\omega_s} = -\frac{q}{m_\mu c}\left[\left(a_\mu + \frac{1}{\gamma_\mu}\right)\vec{B} - \frac{a_\mu \gamma_\mu}{\gamma_\mu + 1}\left(\vec{\beta}\cdot\vec{B}\right)\vec{\beta} - \left(a_\mu + \frac{1}{\gamma_\mu + 1}\right)\vec{\beta}\times\vec{E}\right]. \quad (7)$$

γ_μ is Lorentz factor and a_μ is

$$a_\mu = \frac{g-2}{2}. \quad (8)$$

Now, we think of the case that there is no electric field ($\vec{E} = 0$) and inner product of $\vec{\beta}$ and $\vec{B}$ is negligibly small ($\vec{\beta}\cdot\vec{B} \simeq 0$). Equation 5 and 6 become:

$$\frac{\mathrm{d}\vec{\beta}}{\mathrm{d}t} = -\frac{q}{m_\mu c\gamma_\mu}\vec{B}\times\vec{\beta} = \vec{\omega}_c \times \vec{\beta} \quad (9)$$

$$\frac{\mathrm{d}\vec{s}}{\mathrm{d}t} = -\frac{q}{m_\mu c}\left(a_\mu + \frac{1}{\gamma_\mu}\right)\vec{B}\times\vec{s} = \vec{\omega}_s \times \vec{s}, \quad (10)$$

Note that we introduced two angular momentum vectors ω_c and ω_s. Both vectors are parallel to the magnetic field $\vec{B}$. If we take a difference of these vectors, we have a vector of $g-2$.

$$\vec{\omega}_{g-2} = \vec{\omega}_s - \vec{\omega}_c = -\frac{q}{m_\mu c\gamma_\mu}a_\mu\vec{B} \quad (11)$$

In order to measure measure a_μ precisely, we need to measure ω_{g-2} in the highly precisely adjusted field $\vec{B}$.

EDM term. In case of non-zero electric dipole moment of the muon (μEDM),

$$\vec{d} = \eta_\mu \frac{q}{2m_\mu c}\vec{s}, \quad (12)$$

we have an extra term which should be showed up in spin precession:

$$\vec{\Omega}_{EDM} = \frac{\eta_\mu}{2}\left(\vec{\beta}\times\vec{B}\right). \quad (13)$$

Therefore, angular velocity of spin precession becomes:

$$\vec{\omega} = \vec{\omega}_{g-2} + \vec{\Omega}_{EDM} \quad (14)$$

$$nonumber = -\frac{q}{m_\mu}a_\mu\vec{B} - + \frac{\eta}{2}\left(\vec{\beta}\times\vec{B}\right) \quad (15)$$

We should note that the first term and the second term in Equation 15 are orthogonal each other. Therefore, angular momentum vector $\vec{\omega}$ has a tilt

angle against the magnetic field $\vec{B}$ in the presence of EDM. This tilt angle is an order of 1 mrad, if we take the upper limit of η from the previous experiment E821 [2]. To achieve 100 times better sensitivity, we should be sensitive down to 0.01 mrad of a tilt angle.

Finally in the introduction section, we would itemize three important points to accomplish the new experiment:

- $\left|\vec{E}\right| < 10$mV/cm to avoid spin precession from the electric field less than the order of ppb.
- $\vec{B}$ is precisely adjusted 1 ppm locally and 0.1 ppm in averaged along the orbit,
- inner product of $\vec{B}$ and β should be smaller than 10^{-5} to achieve EDM sensitivity order of 10^{-21}e·cm.

Detailed discussions including R&D status for the first two items are in [5]. In this document we focus on the third item, especially on newly developed three dimensional beam injection scheme for the compact ring. In the following section, we do not describe spin motion but we concentrate on the muon trajectory and the beam dynamics. As long as adiabatic situation, we should be able to follow spin direction by use of Equation 10 Detail discussion of this topic is in [5], and further study is now ongoing.

2. Muon storage ring magnet and injection

The muon storage ring for this experiment will be a precession field 3 Tesla solenoid with cylindrical iron poles and return yoke. The solenoid is being designed now in collaboration with a private company to a specification of $<$ 1 ppm variation of the field locally within the storage region. The storage region, which is defined on the mid-plane, has a radius of 33.3 ± 1.5 cm and height of ± 5 cm, with an applied **weak focusing magnetic field** to keep vertical motion of the beam within a few cm (See section 4). An engineering study for the magnet is discussed in another section. In this section, we introduce three major topics,

- Basic concept of the muon injection strategy,
- Beam physics of 3-D spiral injection,
- Acceptance of the beam at the injection point.

There are two related topics as follows, which are discussed in section 3 and 4.

- Beam transport line
- Weak focusing system and Kicker

2.1. Basic concept of the muon injection strategy

For injection, the muon beam must be injected into the storage ring with minimum interference to the storage field. In the BNL $g-2$ experiment, as displayed in Figure 1, a device called an inflector [6] was used to inject the muon beam into the storage region, to avoid deflection by the fringe field. As the beam crossed the storage region, the beam was kicked horizontally by the kicker to move to the central orbit through an angle large enough to prevent the beam from striking the inflector after one turn. This procedure works only if the radius of the storage ring is large enough compared to the inflector wall thickness. The limitation comes from the required kick-angle within the first turn in the storage ring (within 149.2 ns for BNL case) to avoid hitting the

inflector itself. In the BNL $g-2$ experiment, the radius of storage ring was 711 cm and the wall thickness was $\sim$ 1 cm. Therefore the kick angle was ~ 1.5 mrad.

In our experiment, on the other hand, the radius of the central beam orbit is only 33.3 cm. Using a similar inflector as BNL would require a horizontal kick angle of 30 mrad within the first turn in the ring (within 7.4 ns). This kick angle would be an order of magnitude larger than a kick using any existing technology. Therefore, a horizontal kick does not work for our case.

In order to overcome this difficulty, we have chosen a **spiral injection scheme** instead, as displayed in Fig. 2. At the location where we apply a kick, the beam will be separated from the injecting point by $\sim$40 cm *vertically*, so there would be no disturbance in the incident beam trajectory.

A solenoidal magnet is suitable for this injection scheme as shown in Figure 3. An unique point of this scheme is to build in a radial fringe field to replace the role of the inflector.

The beam momentum is deflected vertically by a radial magnetic field, which will be built in the solenoid fringe field, which is shown as B_R in Fig. 3. The magnetic field should be carefully shimmed not only for the vertical field for the muon storage but also for the radial field so that vertical momentum and position are well controlled throughout the injection volume.

A pulsed magnetic kicker will be used to guide the spiraling beam into a stable orbit at the center of the storage region. The duration of the kick can be for a number of cyclotron (or revolution) periods, since a longer kicker pulse allows a lower kicker voltage and more stability. A multi-turn-kick by the longer pulse shape kicker would be easier.

Finally, the beam is stored into the storage region. In order to control vertical beam motion to within a few cm vertically, we also apply a **weak focusing magnetic field**.

Figure 4 depicts the entire image of solenoid magnet with sample trajectories shown. The beam will enter into the magnet through a hole in the return yoke

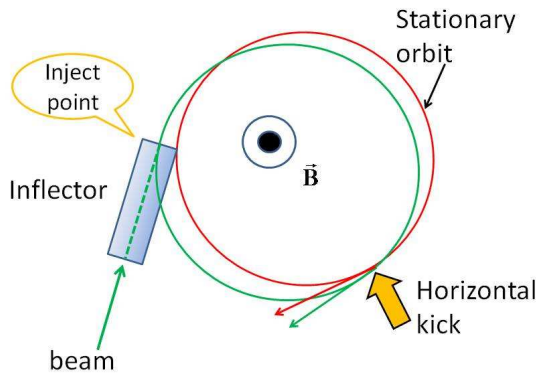

Figure 1: Injection scheme for previous experiment (BNL $g-2$). They use an inflector and horizontal kicker system.

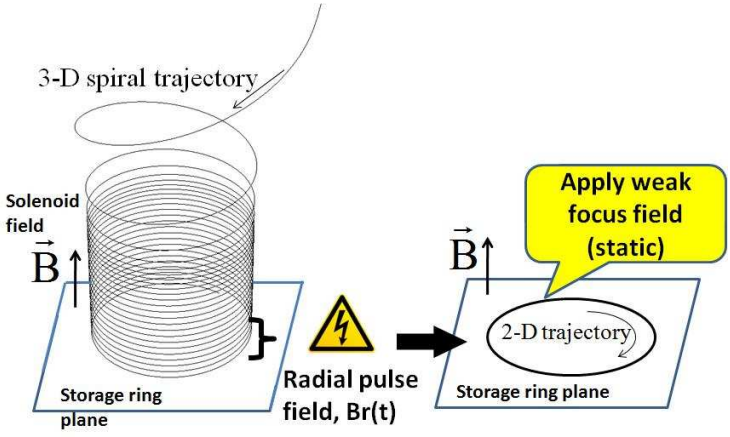

Figure 2: Outline of three-dimensional injection scheme. A radial fringe field deflects the vertical component of the beam momentum to a horizontal component. A pulsed radial magnetic field removes the residual vertical motion down to 10^{-5} [rad], and then a weak focusing field keeps the beam inside the storage area.

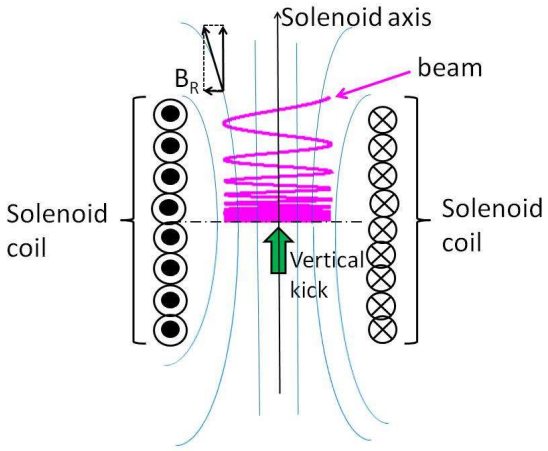

Figure 3: Schematic representation of spiral injection for our case. The method uses solenoid magnet. A radial fringe field, shown as B_R, deflects the vertical component of the beam momentum to a horizontal component.

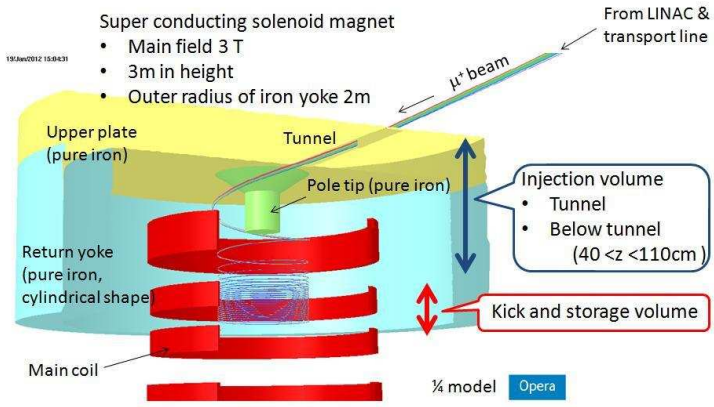

Figure 4: One-quarter cut view of the storage magnet, with sample trajectories shown. The beam enter through a hole in return yoke iron (we call it *tunnel*). Inside the magnet, there are two volumes; **injection volume** (blue double arrow) and **kick and storage volume** (red double arrow).

iron [1], and go through the injection volume (blue double arrow). Then the beam will be kicked vertically and stored into the precise magnetic field (red double arrow). Required precisions of the magnetic field for the injection and storage volume are 100 ppm and 1 ppm locally. Details of the vertical kicker are discussed in Section 4.2.

[1] Note that BNL E821 used a similar hole in the iron return yoke, which was easily compensated for by adding additional iron beside the hole.

2.2. Beam physics of 3-D spiral injection

In this subsection, motion of charged particle(s) in a constant magnetic field is discussed. We use two reference frames (Figure 5). For discussion of the beam inside the storage magnet, we use the lab frame. The beam frame is useful to discuss the beam transport line.

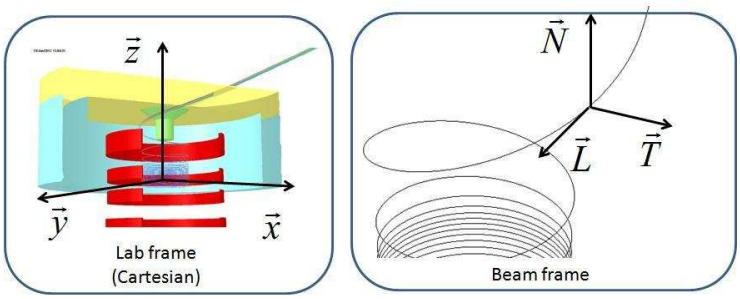

Figure 5: The lab frame and the beam frame are shown.

2.2.1. Kinetics of a single muon in the injection volume (below the tunnel)

The motion of a muon in the presence of a magnetic field, $\vec{B}$, is written as

$$\frac{m_\mu}{\sqrt{1-|V|^2}}\frac{\mathrm{d}^2}{\mathrm{d}t^2}\vec{R} = \frac{q}{m_\mu}\vec{V}\times\vec{B}. \tag{16}$$

Here, $\vec{V}$ and $\vec{r}$ are velocity and position vectors. $\vec{B}$ satisfies

$$\begin{aligned}\nabla\cdot\vec{B} &= 0,\\ \nabla\times\vec{B} &= 0.\end{aligned} \tag{17}$$

In the injection volume below the tunnel, the magnetic field satisfies axial symmetry. The trajectory of a single muon is also axially symmetric. In this document, we take the solenoid axis as the z-axis.

Figure 6 depicts projected trajectory on the $x-y$ plane. The first several turns do not project to a true circle. The position and velocity vectors at an arbitrary **point-A** are written as

$$\begin{aligned}\vec{R} &= (x,y,z) = (R\cos\theta, R\sin\theta, z)\\ \vec{V} &= (V_x,V_y,V_z) = (V_{xy}\cos\phi, V_{xy}\sin\phi, V_z).\end{aligned} \tag{18}$$

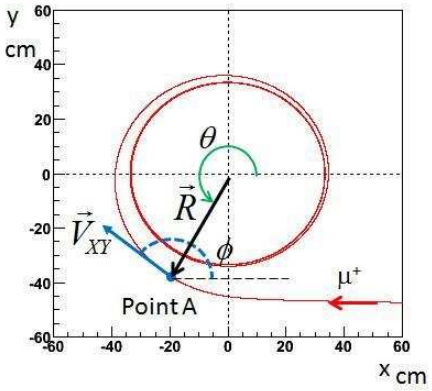

Figure 6: Definitions of $\vec{V_{xy}}$ vector, ϕ and θ angles at an arbitrary point A.

The radial distance and velocity on the $x-y$ plane are $R = \sqrt{x^2+y^2}$ and $V_{xy} = \sqrt{{V_x}^2+{V_y}^2}$ respectively. Note that absolute value of velocity ($V = \sqrt{{V_{xy}}^2+{V_z}^2}$) never changes in the magnetic field.

The axially symmetric magnetic field at **point-A** is given,

$$\vec{B} = (B_x, B_y, B_z) = (B_R\cos\theta, B_R\sin\theta, B_z). \tag{19}$$

B_r and B_y satisfy

$$\frac{\partial B_R}{\partial z} - \frac{\partial B_z}{\partial R} = 0, \tag{20}$$

derived from Equation 17.

Motion of a single muon in the magnetic field is then expressed in time-derivative terms by use of B_R and B_z as

$$\frac{\mathrm{d}V_z}{\mathrm{d}t} = \frac{q}{m_\mu} V_{xy} B_R \sin(\phi-\theta), \tag{21}$$

$$\frac{\mathrm{d}\phi}{\mathrm{d}t} = \frac{q}{m_\mu} B_z. \tag{22}$$

The time rate of change of θ is related to V_{xy} as

$$R\frac{\mathrm{d}\theta}{\mathrm{d}t} = V_{xy}. \tag{23}$$

Note that a projected trajectory is not a true circle in the injection volume as shown in Figure 6. Therefore, distance the R is not the curvature. The curvature ρ is given by

$$\rho = \frac{(x'^2 + y'^2)^{3/2}}{\begin{vmatrix} x' & y' \\ x'' & y'' \end{vmatrix}}, \tag{24}$$

and ρ satisfies

$$\rho \frac{\mathrm{d}\phi}{\mathrm{d}t} = V_{xy}. \tag{25}$$

Here, x' and x'' denote first and second derivatives of time.

Left and right plots in Figure 7 depict B_z (red solid line) and B_R (black solid line) along a trajectory as a function of z. B_R has a local maximum at $z = 81.4$ cm. $B_R \sin(\theta - \phi)$ is also shown in green solid line. The red dotted vertical line indicates $z = 81.4$ cm.

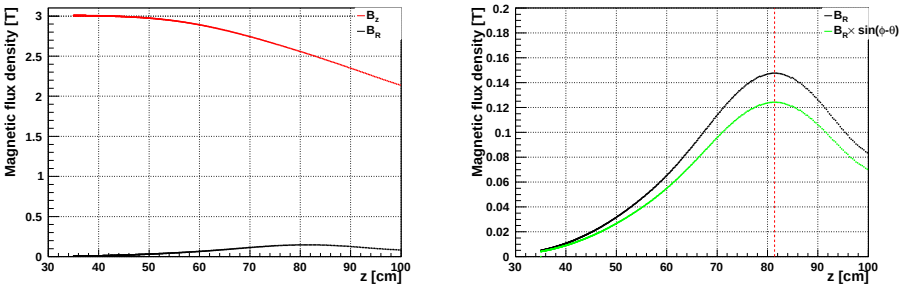

Figure 7: Left: Magnetic field of B_z (main field) and B_R (radial field) along the beam trajectory. Right: Magnified view of B_R and $B_R \times \sin(\phi - \theta)$. Red dotted vertical line indicates $z = 81.4$ cm.

A trajectory given here is a center trajectory of the muon beam. We will discuss how to decide it in the end of this subsection.

Now, we change these time-derivative terms into space-derivative terms. Rewritten, Equation 21 is

$$\frac{1}{V}\frac{\mathrm{d}V_z}{\mathrm{d}z} = \frac{q}{m_\mu}\frac{V_{xy}}{VV_z} B_R \sin(\phi - \theta). \tag{26}$$

Here, we apply

$$\frac{1}{\mathrm{d}t} = \frac{1}{\mathrm{d}z} V_z. \tag{27}$$

The left side plot of Figure 8 depicts values of Equation 26 as a function of z. These values are normalized by V. The right plot depicts V_z/V as a function of z. These values are integrals of the left plot values.

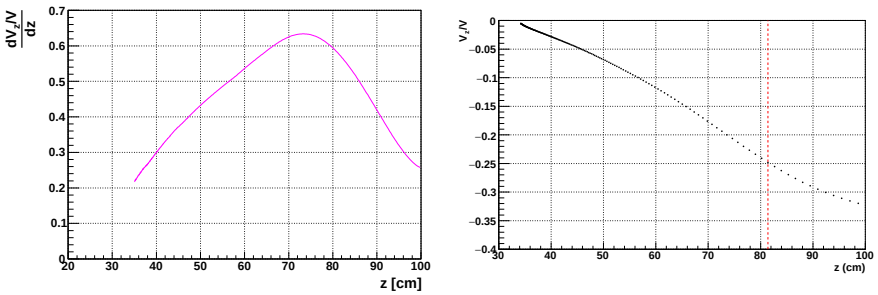

Figure 8: Left: Spatial derivation of V_z (Equation 26) as a function of z. Right:Vertical velocity divided by V. These values are integrals of the left plot values.

Although $B_R \sin(\phi - \theta)$ has a local maximum, the behavior of V_z/V is monotonic. B_z and B_R should change smoothly along the trajectory for smooth injection. The direction of B_R should always be outward to deaccelerate the vertical velocity in the injection volume ($35 \leq z \leq 100$ cm)). In order to estimate the error on B_R in the injection volume, we tried trajectory tracking by changing B_R. We estimate that the error on B_R should be kept within the order of 100 ppm or offset $\leq \pm 2$ Gauss in this injection volume, to control the vertical angle dispersion $\Delta V_z/V \leq \pm 2$ mrad at $z = 35$ cm point. This criteria (± 2 mrad) comes from Figure 20, green line.

The left plot in Figure 9 depicts ρ (in Equation 24) and r as a function of z. As the muon approaches the storage region ($z < 40$), ρ and r come close to 33.3 cm. The right plot in Figure 9 depicts the time rate of change of ϕ and θ. As z approaches below 40 cm, these time rates also approaches the cyclotron angular velocity at B_z=3T:

$$\omega_{cyc} = \frac{q}{m_\mu} B_z = 0.847 \text{ (rad/nsec)}. \tag{28}$$

From this study, we learn the requirements for the magnetic field injection volume ($35 < z < 100$ cm):

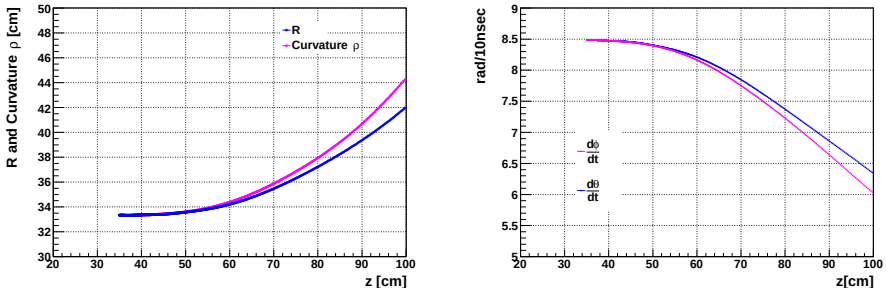

Figure 9: Left: Radial distance on the $x-y$ plane ($R=\sqrt{x^2+y^2}$) and curvature (ρ) as a function of z. Right: Time rate change of ϕ and θ as a function of z. As z approaches the storage region ($z<40$ cm), R and ρ approach the storage radius, 33.5 cm, and both time rates come close to the cyclotron angular velocity at B_z=3T, as shown in Equation 28.

- B_z and B_R should change smoothly along the center trajectory,
- The direction of B_R should be outward,
- Magnitude of B_R as function of z should be determined from the center trajectory,
- The error on B_R should be of order 100 ppm.

Lastly in this subsection, a center trajectory is introduced. There are two requirements; (1) trajectory passes through the tunnel, (2) $V_Z/V \approx -13$ mrad at $z=35$ cm to meet to the capability of the vertical kicker. In order to decide a suitable center trajectory, we tried **reverse** trajectories with several models of magnet. By use of a certain given model, we calculated **reverse** trajectory which starts at $z=35$ cm, and its initial pitch is $V_Z/V=13$ mrad. Then we tried modification of a tunnel design in the upper yoke plate till a trajectory passes through smoothly. Round shape cross section is better to minimize disturbance of the magnetic field inside a yoke ($z<110$ cm). We determine tunnel radius is 40 mm for straight cylinder shape. Once we decide a trajectory, requirements of spatial distribution of the magnetic field are also automatically obtained.

However, how do we design practical shape of magnet to meet magnetic field requirements? This is an one of two crucial points to judge feasibility of the

3-D spiral injection scheme. The MRI design technology allows us to calculate specific parameters of magnet (coil shape, current density distribution, yoke shape, and so on), if we specify spatial distribution of the magnetic field. Details of this technology is discussed in [7, 8].

The second crucial point is how large acceptance is allowed for the 3-D spiral injection. We need to consider phase space matching at the entrance point the tunnel in the upper yoke plate with careful consideration of the vertical kicker and the weak focusing field. We will discuss how to estimate acceptance of the beam injection in the following sections.

2.2.2. Spatial correlation around a base trajectory (below the tunnel)

Figure 10 depicts 20 trajectories (red lines) around a base (or reference) trajectory (black solid line). A zoom in view is on the right. Reference trajectory is one of the best **inverse** trajectory samples of a single muon, starting from the center of solenoid magnet to the tunnel in the upper end plate. To find a base trajectory and appropriate tunnel geometry, we repeated inverse tracking computations as muon goes along the center line in the tunnel. Red sample trajectories are also obtained by inverse computation changing initial positions of **inverse** trajectory. Each trajectory satisfies the correlations developed in Equations 21− 25.

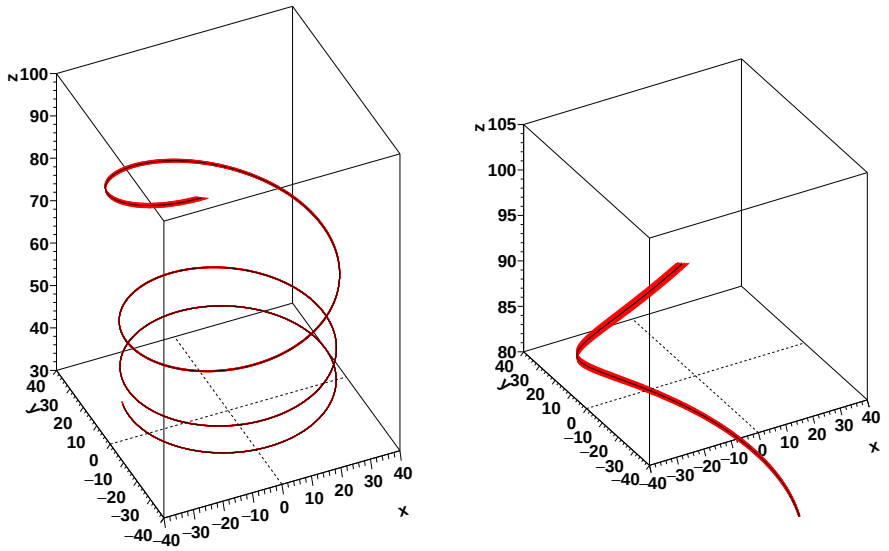

Figure 10: A base trajectory (black solid line) and good sample trajectories (red solid lines) in the injection volume, below the tunnel are shown. A magnified view is on the right.

Sliced views around z=100 cm are shown in Figure 11. Here, $r = \sqrt{x^2 + y^2}$ and definitions of ϕ and θ were introduced in Figure 6. These plots indicate linear correlations around a base trajectory. Because the magnetic field below the tunnel volume is axially symmetric, the trajectories also satisfy axial symmetry.

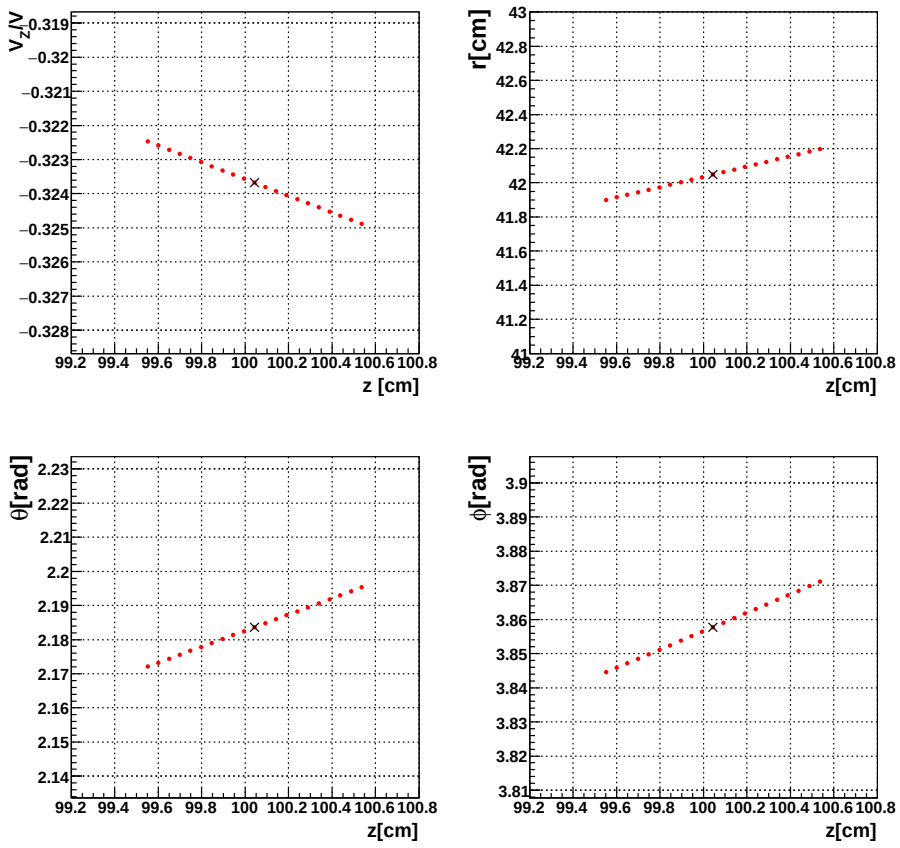

Figure 11: Sliced views around $z = 100$ cm. Black point is the base trajectory. Red points correspond to twenty good samples around the base. $R = \sqrt{x^2 + y^2}$ and the definitions of ϕ and θ are introduced in Figure 6. We find linear correlations around the base trajectory.

Average slopes of these correlations in Figure 11 are obtained as follows:

$$\left\langle \frac{\Delta r}{\Delta z} \right\rangle = \frac{1}{20} \sum_{i=-10}^{10} \frac{R^i - R^0}{z^i - z^0},$$
$$\left\langle \frac{\Delta V_z/V}{\Delta z} \right\rangle = \frac{1}{20} \sum_{i=-10}^{10} \frac{({V_z}^i - {V_z}^0)/V^0}{z^i - z^0},$$
$$\left\langle \frac{\Delta \theta}{\Delta \tau} \right\rangle = \frac{1}{20} \sum_{i=-10}^{10} \frac{\theta^i - \theta^0}{(z^i - z^0)/{V_z}^0},$$
$$\left\langle \frac{\Delta \phi}{\Delta \tau} \right\rangle = \frac{1}{20} \sum_{i=-10}^{10} \frac{\phi^i - \phi^0}{(z^i - z^0)/{V_z}^0}. \tag{29}$$

Values in parentheses $\langle \cdots \rangle$ are average values of 20 sample trajectories and the superscript 0 represents the base trajectory. $\Delta\tau$ relates to vertical displacement divided by ${V_z}^0$. Average correlation slopes are compared with equations of a single base trajectory (Equations 26, 22 and 23) as follows:

$$\left\langle \frac{\Delta r}{\Delta z} \right\rangle \Rightarrow \frac{\mathrm{d}r}{\mathrm{d}z}, \tag{30}$$

$$\left\langle \frac{\Delta V_z/V}{\Delta z} \right\rangle \Rightarrow \frac{\mathrm{d}V_z/V}{\mathrm{d}z}, \tag{31}$$

$$\left\langle \frac{\Delta \theta}{\Delta \tau} \right\rangle + \omega_{cyc} \Rightarrow \frac{\mathrm{d}\theta}{\mathrm{d}t}, \tag{32}$$

$$\left\langle \frac{\Delta \phi}{\Delta \tau} \right\rangle + \omega_{cyc} \Rightarrow \frac{\mathrm{d}\phi}{\mathrm{d}t}. \tag{33}$$

The left plot of Figure 12 depicts $\langle \Delta r/\Delta z \rangle$ as a function z in green filled circles. The blue solid line is $\mathrm{d}r/\mathrm{d}t$ from a base trajectory for comparison. They are in good agreement. Similarly, the right plot depicts $\langle \Delta(V_z/V)/\Delta z \rangle$ as a function of z in blue filled circles. The pink line is $(\mathrm{d}V_z/V)/\mathrm{d}z$ from a base trajectory. Figure 13 depicts the angular velocities of ϕ and θ as a function of z. Open circles are $\langle \Delta\theta/\Delta\tau \rangle$ and $\langle \Delta\phi/\Delta\tau \rangle$. Solid lines are $\mathrm{d}\phi/\mathrm{d}t$ and $\mathrm{d}\theta/\mathrm{d}t$ from a single trajectory. We have introduced $\Delta\tau$ instead of Δz in order to compare with $\mathrm{d}\theta/\mathrm{d}t$ and $\mathrm{d}\phi/\mathrm{d}t$

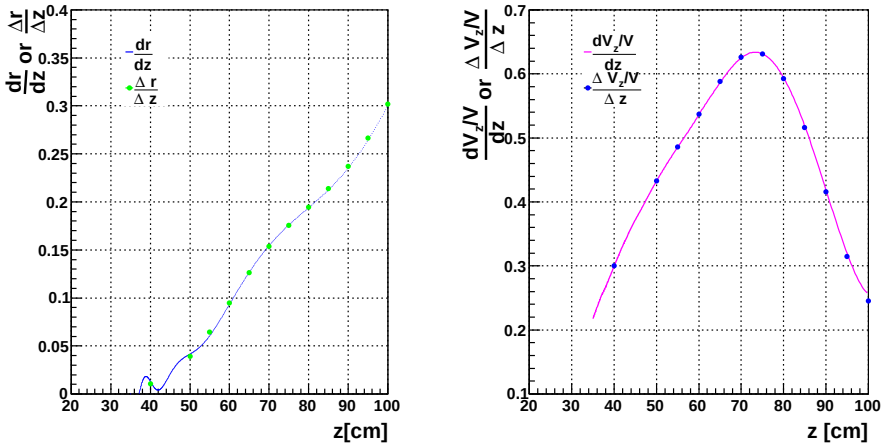

Figure 12: Left: Comparison between $\langle \Delta r/\Delta z \rangle$ vs. $\mathrm{d}r/\mathrm{d}z$ in Equation 30. Right: Comparison between $\langle (\Delta V_z/V)/\Delta z \rangle$ vs. $(\mathrm{d}V_z/V)/\mathrm{d}z$ in Equation 31. Slopes of the linear correlations around the base trajectories are consistent with spatial derivations of the single base trajectory (inside the injection volume below the tunnel).

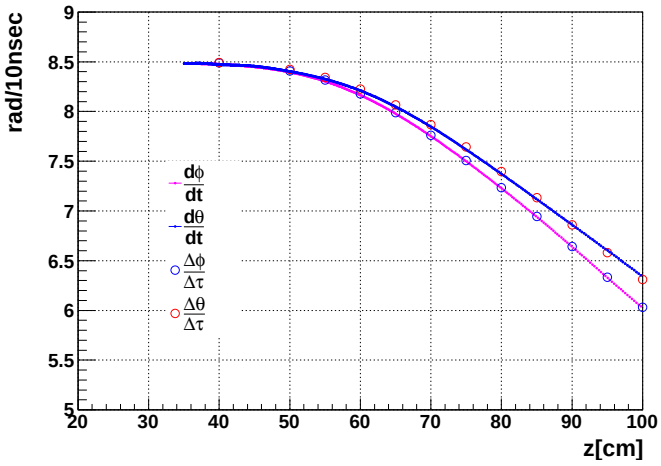

Figure 13: Comparisons between $\langle \Delta\phi/\Delta\tau \rangle$ vs. $\mathrm{d}\phi/\mathrm{d}t$ in Equation 32, and $\langle \Delta\theta/\Delta\tau \rangle$ vs. $\mathrm{d}\theta/\mathrm{d}t$ in Equation 33.

In this way, we have introduced linear correlations around a base trajectory, and confirmed that these correlations are consistent with time-derivative or spatial derivative terms of a single base trajectory as shown in Figure 12 and 13. Linear correlations are valid as long as the magnetic field is axially symmetric, below the tunnel volume.

The next step is to study whether these linear correlations still describe the trajectories inside the tunnel. The magnetic field inside the tunnel will be small, but it changes field profile dramatically. Moreover, the field is not axially symmetric anymore.

2.2.3. Trajectories inside the tunnel

There will be a tunnel in the upper end plate of the storage magnet, in order to pass the muon beam from the exit of transport line into the storage magnet. Figure 14 depicts a cut view of the tunnel with sample trajectories. The magnetic field strength is also shown in colored contour. Field changes dramatically at the tunnel exit. Left and right plots in Figure 15 depict the geometric form of the tunnel. Tunnel entrance and exit points are at $z = 145$ cm and $z = 110$ cm, respectively. The tunnel is a straight cylinder shape with a radius of 35 mm.

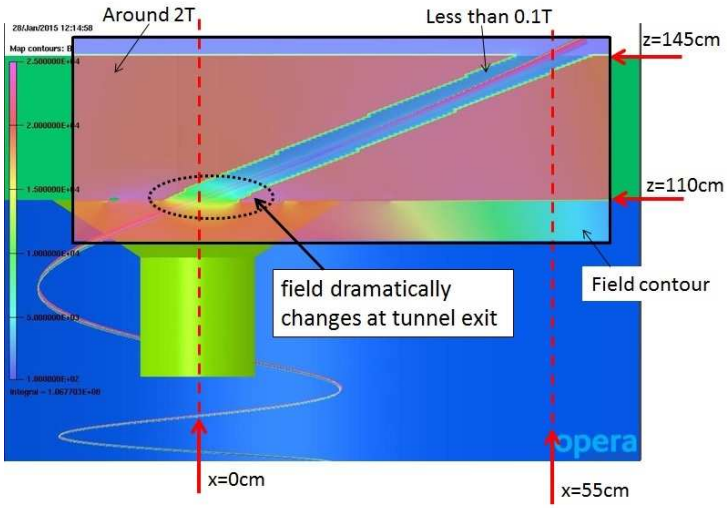

Figure 14: Closer cut view of the tunnel. Red arrows show geometric information. The magnetic field strength is also shown in colored contour. As we emphasize in the dotted ellipse, the field changes dramatically at the tunnel exit.

Figure 16 and 17 depict the magnetic field profile of B_z, B_x and B_y along the base trajectory as a function of z. We set five 3-dimensional straight lines through the tunnel to see the field profile. One is along geometric center of tunnel, and another four lines are displaced in parallel. The field profile along the center line is aqua blue. Green and black lines depict the field profile along displaced lines in the z direction $\pm$ 2 cm. Orange and purple lines depict field

profile along displaced lines in the y direction ± 2 cm. B_z changes by 2 T between $105 \leq z \leq 115$ cm (Figure 16) and B_x and B_y have non-linear behavior (Figure 17). B_x, B_y and B_z for $z \geq 120$ cm are smaller than 0.1 T. Inside the tunnel is not a simple drift space, and we look at trajectories in the next.

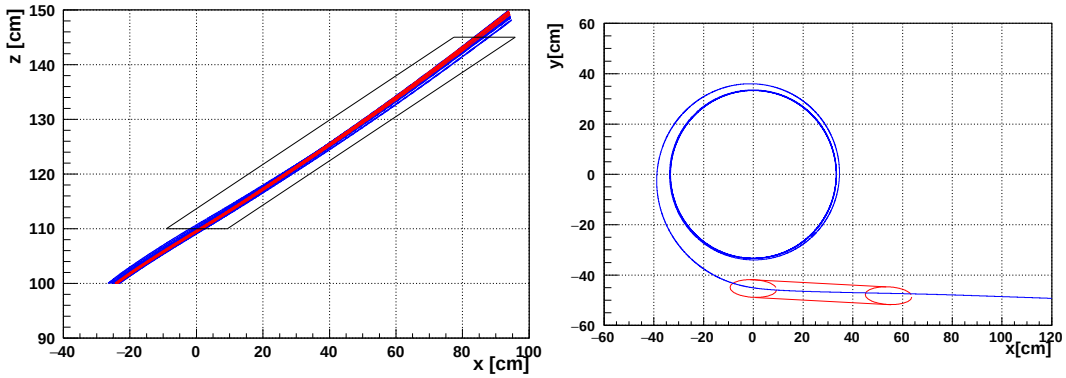

Figure 15: Geometric form of the tunnel is shown in red solid line. The base trajectory is also shown. X-Z view in the left and X-Y view is in the right.

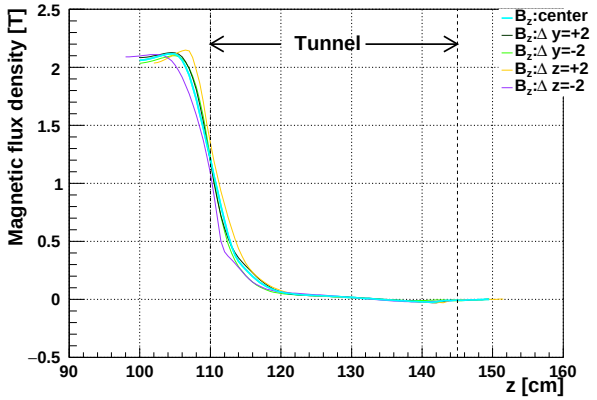

Figure 16: Magnetic field profile (B_z) as a function of z. Several profiles are along three dimensional straight lines. Blue is along the geometric center of the tunnel, the other four lines are displaced in $\pm\Delta y$(horizontally) and $\pm\Delta z$ (vertically) directions.

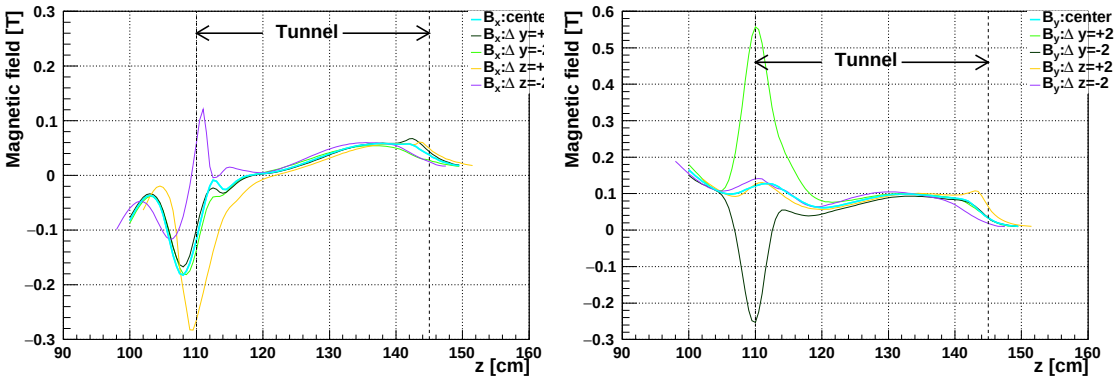

Figure 17: Left: Field profiles for B_x, with blue along the tunnel center. Right: Same for for B_y.

First we check whether linear correlations are still useful descriptions inside the tunnel. Figure 18 depicts beam shapes at $z = 100, 110, 120, 140$ and 150 cm in different colors. In order to compare beam shape at different z points, we plot relative differences compared with the base trajectory. As we saw in Figure 11, the beam shape is linear around the base trajectory at the $z = 100$ cm point (below the tunnel; magnetic field satisfies axial symmetry). However, the beam shapes lose linearity as z increases. Correlations are not linear anymore at $z \geq 120$ cm. It is clear especially in the $\Delta z - \Delta\phi$ plot. But, if we take trajectories within $|\Delta z| \leq 0.5$ cm in Figure 18, we find reasonably "linear phase-space" shape even at the $z = 150$ cm point. Therefore we can utilize this feature to determine the desired beam shape at the exit point of the beam transport line as we will discuss in subsection 3.

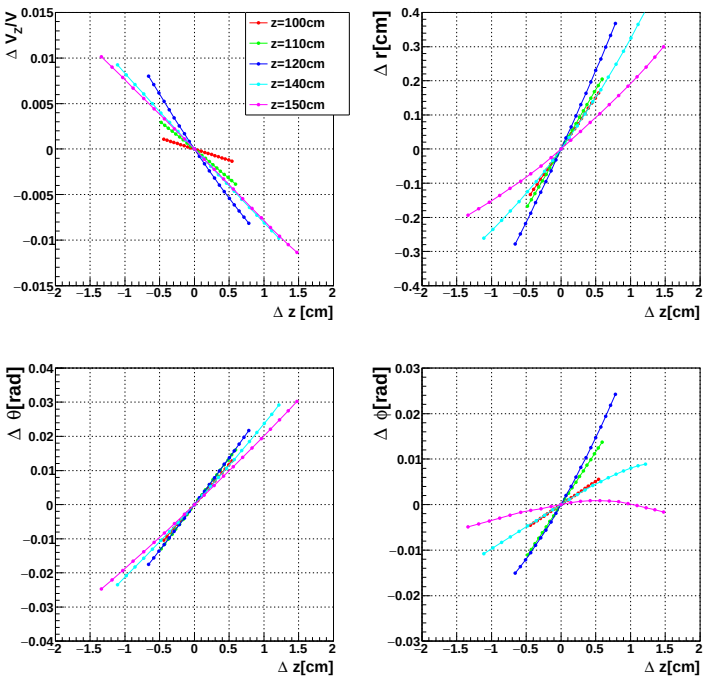

Figure 18: Beam shapes at $z = 100 \sim 150$ cm. These are similar plots of Figure 11. But we plot relative differences compared with the base trajectory.

2.3. Acceptance of the beam at the injection point

In this subsection, we estimate the acceptance of the beam at the injection point ($z = 150$ cm). Inside the acceptance, the beam should satisfy the criteria for good storage.

Figure 19 depicts sample trajectories (left) and the $y - z$ coordinate of each trajectory near the injection point (right). We set more than 6000 trajectories. Each colored area contains fifty trajectories. The red solid line corresponds to the correlation, which we introduced in the previous sections. We can express this red line as follows:

$$z = p \times y + q, \tag{34}$$

here p and q are slope and intercept parameters. Samples in each colored area are obtained by changing y and q values by 0.5 mm interval. Therefore, these all samples satisfy such linear correlations.

Most of sample trajectories go through the tunnel, but some of them are reflected inside the storage volume because of an weak focusing field. As we mentioned briefly in subsection 2.1, there is an weak focusing field in storage volume (see Figure 2). And we apply vertical kick around $z = 35$ cm, in order to kick the beam into the storage volume. Therefore, we need to set a criteria to meet requirements of the kicker system and weak focusing field.

Figure 20 depicts z vs.$\Delta V_z/V$ plot around $z = 35$ cm. The green region meets the criteria of good kick and stable storage. Details of this estimation are discussed in section 4. The red envelope in the right plot of Figure 40 corresponds to the green region in Figure 20. We may accept the black region as good trajectories, here.

Black dots on the right side plot in Figure 21 depicts $y-z$ cut view of selected trajectories near the injection point. There are 207 trajectories. Left side plot depicts the selected trajectories above kick point ($z \sim 35$ cm). Figure 22 depicts geometric information of kicker coils and trajectories. Zoom up is in the right plot. Details of the kicker system are discussed in Section 4.2.

Now we take a closer look of the beam shape at the injection point. Selected

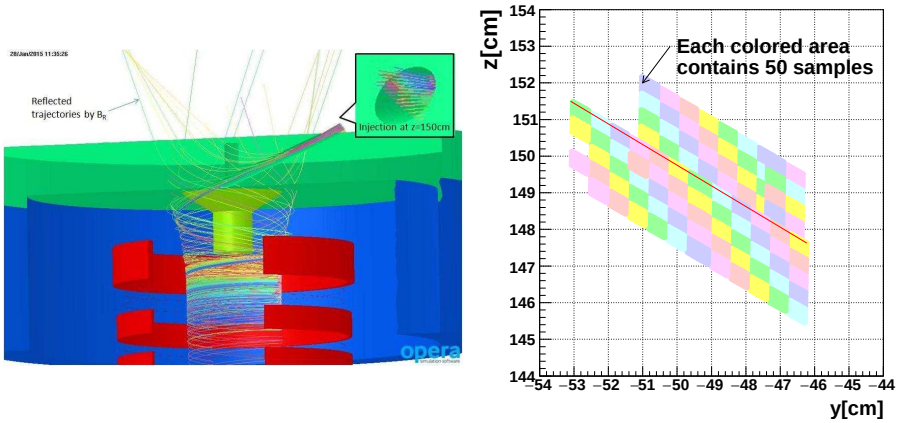

Figure 19: Sample trajectories and $y-z$ cross section at the injection point. There are more than 6000 trajectories. Each colored area in the quilt contains fifty trajectories. They satisfy linear phase-space correlations, which we introduced in the previous sections (red solid line).

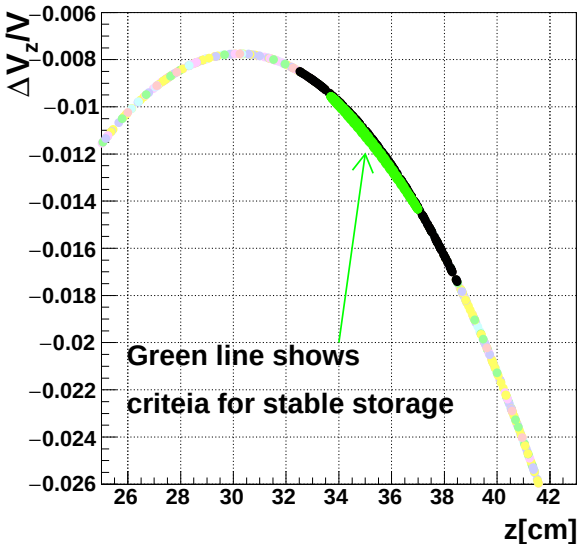

Figure 20: Correlation of z vs.$\Delta V_z/V$ around $z = 35$ cm is shown. A criteria to meet requirement from kicker system and good storage inside a weak focusing field is shown in green line. This green line corresponds to red envelope in the right side plot of Figure 40. We may accept the black region as good trajectories, here.

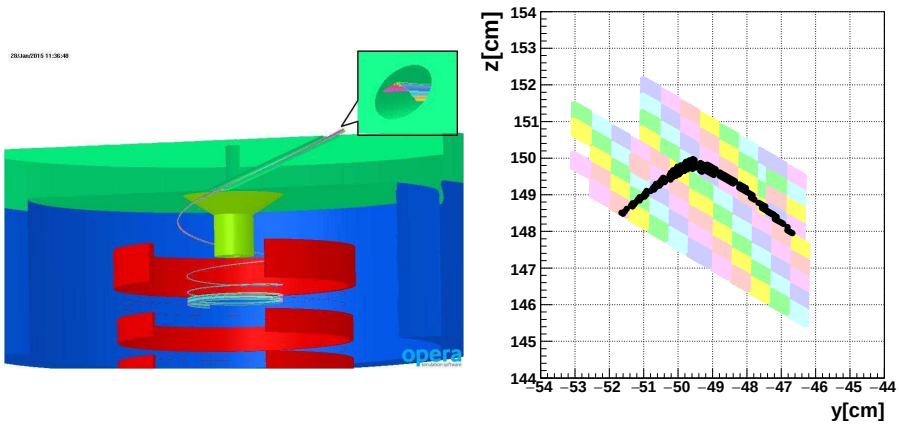

Figure 21: Similar plot to Figure 19 but we show selected trajectories. Black dots on the right side plot depict a $y - z$ cut view of selected trajectories at the injection point. There are 207 trajectories.

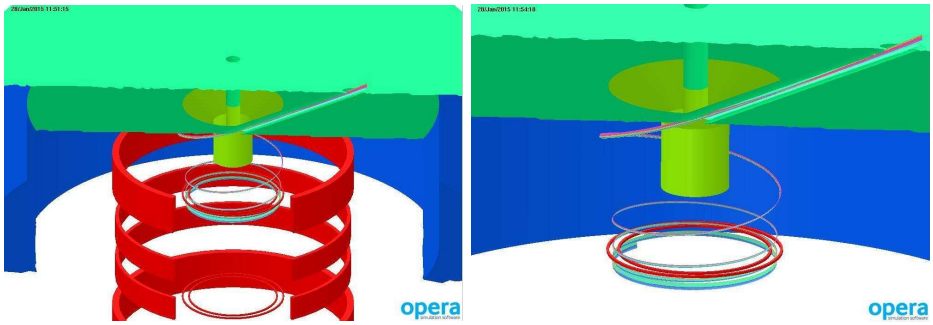

Figure 22: Geometric information of the kicker coils as well as good sample trajectories. A magnified view with the upper kicker coils is shown in the right. The beam passes **between** the upper kicker coils. The radial distance between the two coils is 6 cm.

trajectories are shown in black dots in Figure 23, like a boomerang shape. These black boomerangs correspond to the beam acceptance at the injection point. Similarly, the four plots in Figure 24 also show the beam shape in **the beam frame** (See Figure 5). We change the coordinate system because the beam frame is useful to design the beam transport line. We select the relatively linear areas shown on Figure 24 and set them as *target beam shapes*. We design the beam transport line to meet these target shapes (see section 3).

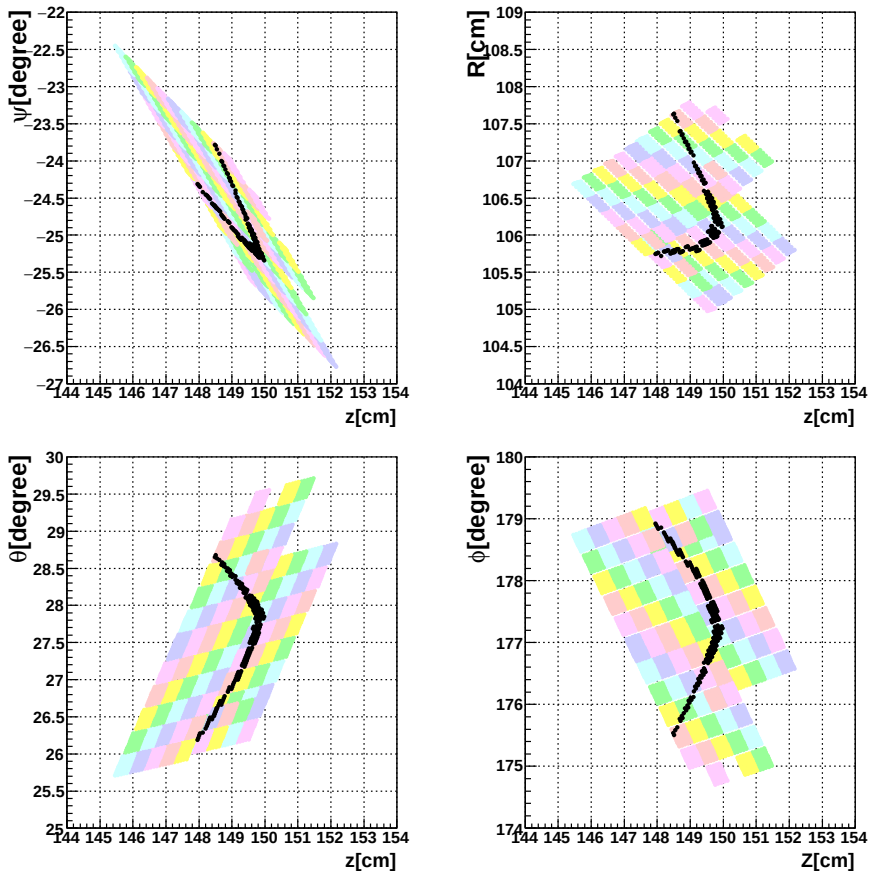

Figure 23: Beam shapes at the injection point. Black dots areas, which look like a boomerang, are selected trajectories. These boomerangs correspond to the beam acceptance at the injection point.

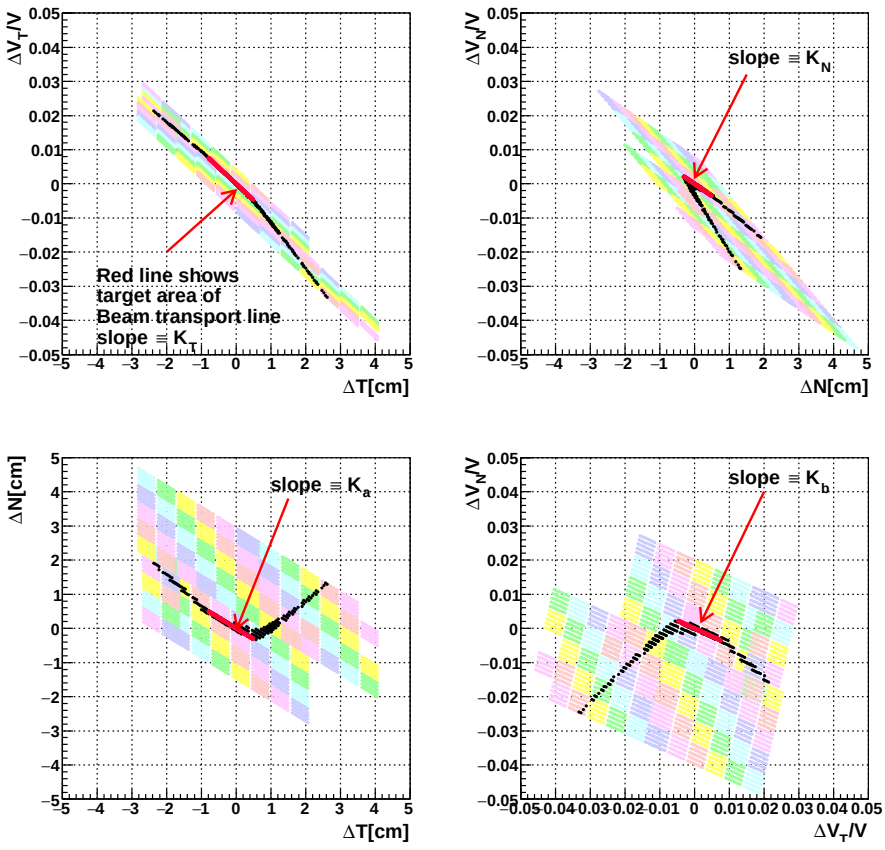

Figure 24: Similar plots to Figure 23, but using **the beam frame**. We select relatively linear area around red lines as *target beam shapes*. Slope values of red lines (K_T, K_N, K_a and K_b) are introduced in Figure 31 in section 3. We design the beam transport line to meet these target shapes.

Before we move to a discussion of the beam transport line design, we should look at the selected trajectories inside the tunnel. Blue and red solid lines in Figure 25 are selected trajectories. Red line trajectories correspond to roughly the *target beam shape*. The black line is the tunnel shape. As shown in the right side plot in Figure 25, red line trajectories gather around the geometric center of the tunnel exit.

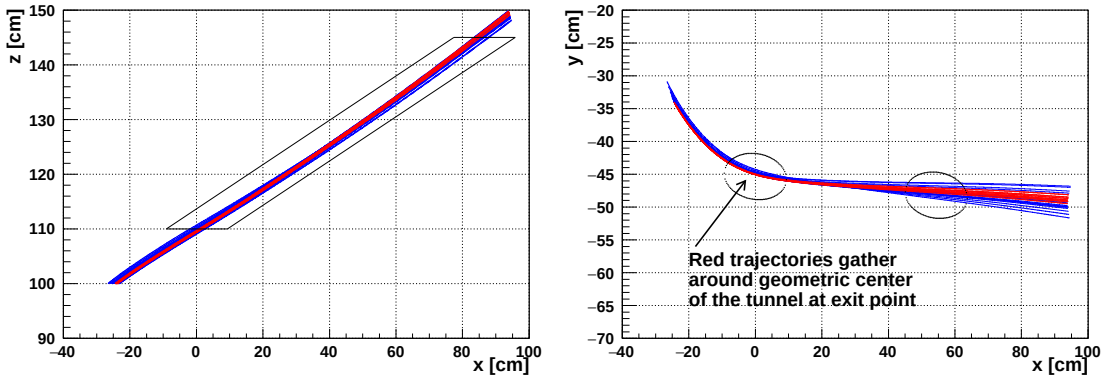

Figure 25: Left: The $x - z$ view of the selected trajectories (blue and red solid lines) inside the tunnel are shown. Red line trajectories correspond to around *target beam shape*. Black line is tunnel shape. Right: Same for The $x - y$ view.

Figure 26 and 27 depict the magnetic field profile *along* trajectories. Blue and red solid lines correspond to trajectories which are introduced in Figure 25.

For comparison, magnetic field profile along 3-dimensional straight lines (which are introduced in Figure 16 and 17 are also shown. The selected trajectories (red) are not much affected by B_x and B_y.

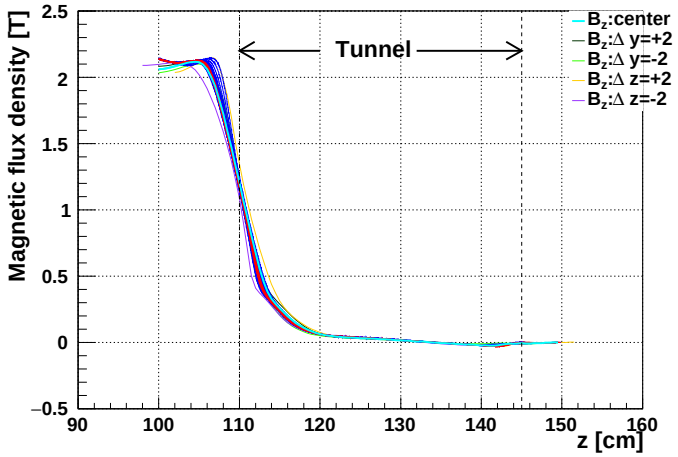

Figure 26: Magnetic field profile of B_z *along* trajectories are shown. Blue and red solid lines correspond to trajectories in Figure 25. For comparison, the magnetic field profile along 3-dimensional straight lines (which are introduced in Figure 16 and 17 are shown.

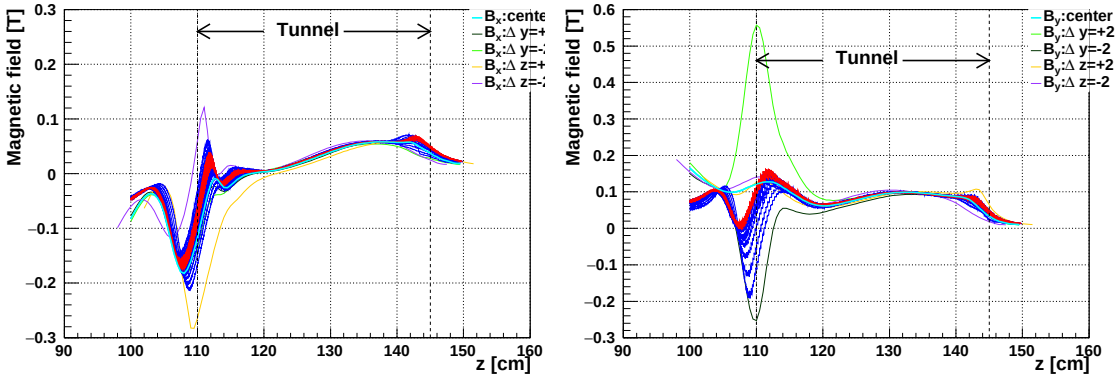

Figure 27: Left and Right are the same as Figure 26, for B_x and B_y respectively. Selected trajectories (red) see a small B_x and B_y.

3. Beam Transport Line

In this section, we discuss the beam transport line from the LINAC exit to the injection point of the storage magnet. Figure 28 and 29 depict schematic views. Most parts of transport line are tilted along a 25° slope to meet the requirement of beam injection. The difference in height is more than 3 m between the start and end points. The transport line can be divided into three major parts as follows.

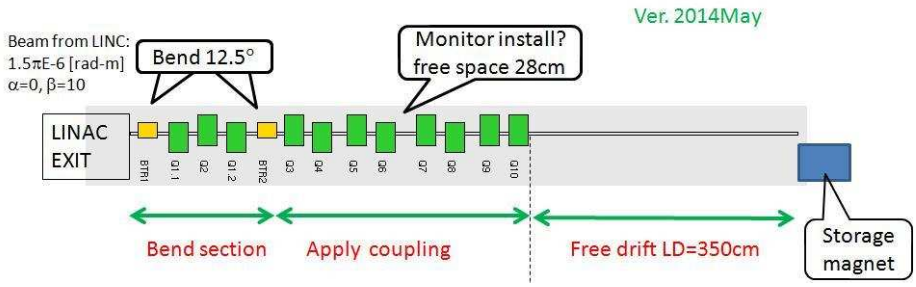

Figure 28: Schematic view of the beam transport line. This transport line connects between the exit of the LINAC and the injection point of the storage magnet. The beam line consists in mainly three parts: beam bending section, transverse-normal coupling section and free drift section.

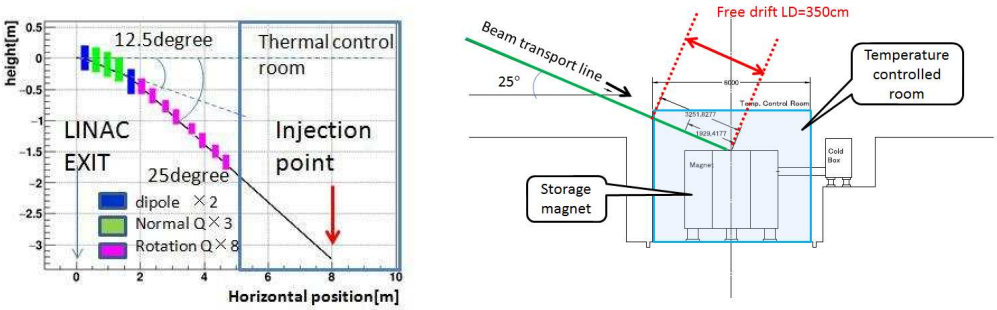

Figure 29: Left: Difference in height between the start and end points is shown. Right: Free drift space inside the temperature controlled room is shown. The injection point is just above the upper yoke of the storage magnet.

Beam bending section. In order to bend the muon beam by 25° vertically, and minimize vertical energy dispersion, there are two dipole magnets and three quadrupole magnets in this section. Each dipole magnet bends the beam by 12.5°.

Transverse and normal coupling section. As we discussed in section 2, strong coupling between transverse and normal (vertical) components is required from the 3−D spiral injection scheme. We apply appropriate coupling in this section by use of eight rotated quadrupole magnets.

Free drift space section. As shown in the right plot in Figure 29, the storage magnet is inside a constant temperature room. Therefore, this transport line needs to include 3.5 m of free drift space. In principle, we do not plan to put any massive equipment (magnets) inside the constant temperature room.

However, we would mention about fraction of muon decay loss. Time of flight of the muon beam from the entrance of beam transport line to kick point in the storage magnet is 67 nsec. The transport line is 8.5 m and, 5 turns in the injection volume (see Figure 10). Therefore, decay loss in the entire injection path is:

$$\epsilon = 1 - \exp\left(-\frac{67\text{nsec}}{6.6\mu\text{sec}}\right) \cong 0.0101, \tag{35}$$

here 6.6 μsec is the lifetime of the muon ($\gamma_\mu = 3$).

In this section, we use the beam frame, which denotes $\vec{L}$ as beam direction and $\vec{T}$ as transverse direction as shown in right side picture of Figure 5. $\vec{T}$ stays always on the x-y plane in the lab frame. $\vec{N}$ is an outer product of $\vec{L}$ and $\vec{T}$.

3.1. Transfer matrix of transport line

The transfer matrix M is introduced here. $\vec{X}_{in}$ and $\vec{X}_{out}$ are the phase space at the entrance and exit points. They are related as:

$$\vec{X}_{out} = M\vec{X}_{in}, \tag{36}$$

and

$$\vec{X}_{in/out} = \begin{bmatrix} \Delta T \\ \Delta V_T/V \\ \Delta N \\ \Delta V_N/V \end{bmatrix}_{in/out} . \quad (37)$$

This four-by-four matrix M reflects the beam motion in normally ($\vec{N}$) and transversely ($\vec{T}$). Here, we do not treat the longitudinal component of the beam. ΔT and ΔN are positional displacements from the center of the beam. $\Delta V_T/V$ and $\Delta V_N/V$ are relative differences of beam velocity from the center values of the beam.

In general, the transfer matrix M is obtained from Twiss parameters at the entrance and exit points of the transport line. M is written as:

$$\begin{aligned} M &= {U_{out}}^{-1} D, \\ U_{out} &= \begin{bmatrix} \mu & 0 & -R_4 & R_2 \\ 0 & \mu & R_3 & -R_1 \\ R_1 & R_2 & \mu & 0 \\ R_3 & R_4 & 0 & \mu \end{bmatrix}, \\ D &= \begin{bmatrix} D_T & 0 \\ 0 & D_N \end{bmatrix}. \end{aligned} \quad (38)$$

Here, U_{out} is a 4×4 rotation matrix at the exit of the transport line. U_{out} consists in four independent values of R_1, R_2, R_3, and R_4. These are the coupling parameters. They indicate the strength of coupling between normal and transverse beam motion. Because the parameter μ is defined as $\mu = \sqrt{1 - (R_1 R_4 - R_2 R_3)}$, rotation matrix U_{out} is symplectic. In the case of a decoupled beam, $R_1 \sim R_4$ are all zero, and hence the rotation matrix is an identity matrix. (That is why we do not discuss the rotation matrix at the entrance of the beam transport line, U_{in} in Equation 38.)

Matrix D is a 4×4 block diagonal matrix. It consists in 2×2 matrices of

D_T and D_N. D_T is expressed as follows:

$$D_T = \begin{bmatrix} \frac{1}{\sqrt{\beta_T{}^{out}}} & 0 \\ \frac{\alpha_T{}^{out}}{\sqrt{\beta_T{}^{out}}} & \frac{1}{\sqrt{\beta_T{}^{out}}} \end{bmatrix}^{-1} \Phi_T \begin{bmatrix} \frac{1}{\sqrt{\beta_T{}^{in}}} & 0 \\ \frac{\alpha_T{}^{in}}{\sqrt{\beta_T{}^{in}}} & \frac{1}{\sqrt{\beta_T{}^{in}}} \end{bmatrix}. \tag{39}$$

$\alpha_T{}^{in(out)}$ and $\beta_T{}^{in(out)}$ are Twiss parameters of the transverse elements at the entrance (or exit) point. The 2×2 matrix Φ_T is related to the phase advance and is expressed as:

$$\Phi_T = \begin{bmatrix} \cos\phi_T & \sin\phi_T \\ -\sin\phi_T & \cos\phi_T \end{bmatrix}. \tag{40}$$

We fix $\phi_T = 0$ now, because ϕ_T does not affect on the beam shape at the exit point. D_N is written in the same way as D_T, but with normal (N) Twiss parameters, also we set $\phi_0 = 0$.

In order to determine the transfer matrix M, we need to set the Twiss parameters at the entrance and exit points. The Twiss parameters at the entrance point are given by the LINAC design, and are listed in Table 2.

Table 2: Beam parameters at the entrance of transport line (the exit of LINAC)

emittance [rad-m]	$\epsilon_T = 1.5\pi \times 10^{-6}$
	$\epsilon_N = 1.5\pi \times 10^{-6}$
Twiss parameters	$\alpha_T{}^{in} = 0.0$, $\beta_T{}^{in} = 10.0$
	$\alpha_N{}^{in} = 0.0$, $\beta_N{}^{in} = 10.0$

In general, as long as there is no coupling between the $\vec{T}$ and $\vec{N}$ components, the average beam size is directly related to the Twiss parameters:

$$\begin{aligned} \alpha_T &= \frac{\langle \Delta T \cdot \Delta V_T / V \rangle}{\epsilon_T}, \\ \beta_T &= \frac{\langle \Delta T^2 \rangle}{\epsilon_T}, \\ \frac{1+\alpha_T{}^2}{\beta_T} &= \frac{\langle \Delta V_T{}^2 \rangle}{\epsilon_T}. \end{aligned} \tag{41}$$

The same goes for $\vec{N}$ components.

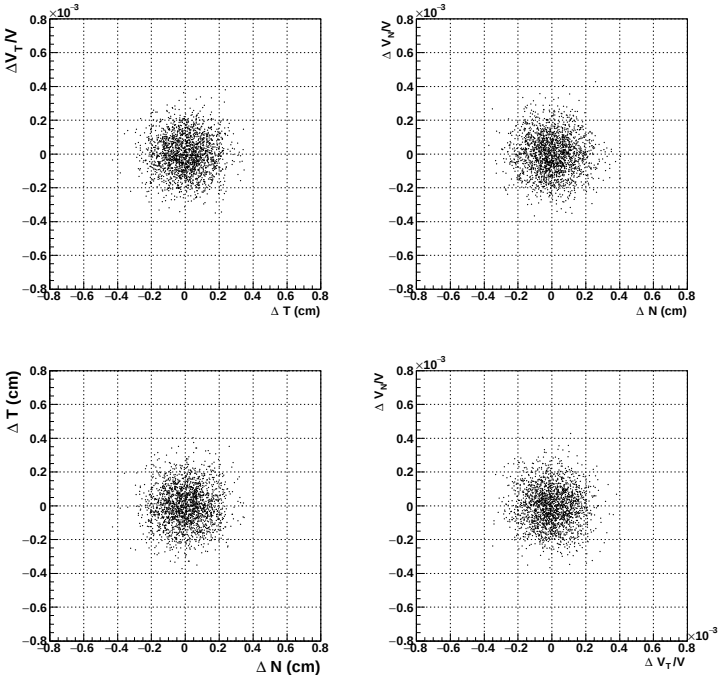

Figure 30: The beam phase space at the entrance point is shown. There are 2000 samples. Because ${\alpha_T}^{in}$ and ${\alpha_N}^{in}$ are zero, the phase spaces of (ΔT vs. $\Delta V_T/V$) and (ΔN vs. $\Delta V_N/V$) have no correlation. We assume the beam shape is Gaussian transversely and normally.

Because ${\alpha_T}^{in}$ and ${\alpha_N}^{in}$ are zero, the phase spaces (ΔT vs. $\Delta V_T/V$) and (ΔN vs. $\Delta V_N/V$) have no correlation. We assume the beam shape is Gaussian transversely and normally. Figure 30 depicts the beam phase space at the entrance point. 2000 sample events are shown.

Twiss parameters at the exit of beam transport line. Figure 31 depicts the beam shape at the exit of the transport line. The Red lines in Figure 31 are target slopes which we have introduced in Figure 24. Especially, the two slopes of upper the two plots, which we call K_T and K_N, are directly connected to the Twiss parameters. Twiss parameters at the exit point are obtained as follows:

$$\begin{aligned} {\alpha_T}^{out} &= K_T \times {\beta_T}^{in}, \quad {\beta_T}^{out} = {\beta_T}^{in}, \\ {\alpha_N}^{out} &= K_N \times {\beta_N}^{in}, \quad {\beta_N}^{out} = {\beta_N}^{in}, \end{aligned} \tag{42}$$

here, we set ${\beta_N}^{out}$ and ${\beta_T}^{out}$ with no change.

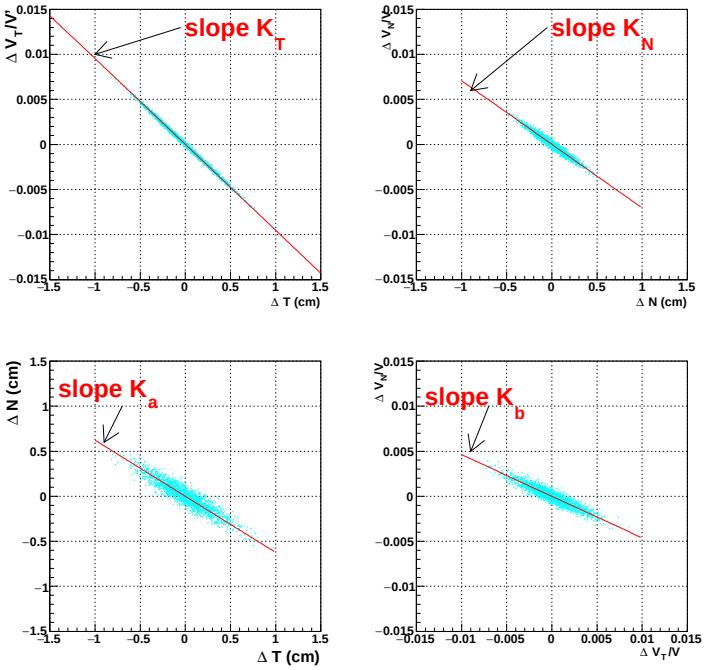

Figure 31: Beam shape at the exit of the transport line is shown. We apply matrix M with sample events shown in Figure 30. The red lines are target slopes which we have introduced in Figure 24. Four slopes, which we call K_T, K_N and K_A and K_b, are connected to Twiss parameters.

Table 3 shows the Twiss parameters at the exit of transport line.

Now, we discuss how to estimate the coupling parameters $R_1 \sim R_4$. The two

Table 3: Beam parameters at the exit of the transport line (the injection point)

Twiss parameters	Coupling parameters
${\alpha_T}^{out} = 9.50$, ${\beta_T}^{out} = 10.0$	$R_1 = -1.03$,$R_2 = -1.49$
${\alpha_N}^{out} = 7.06$, ${\beta_N}^{out} = 10.0$	$R_3 = -0.86$,$R_4 = -0.61$

slopes of the bottom two plots in Figure 31, which we call K_a and K_b, connect to the coupling parameters $R_1 \sim R_4$. However, an analytical calculation is difficult. Therefore, we use an iterative calculation method using a simple model.

We set an input beam shape as a circle with radius is 5 mm, and set an initial momentum spread of zero for both transverse and normal components. The black solid lines in Figure 32 depict the input beam shape, and the red lines are the target slopes. Then we set arbitrary $R_1 \sim R_4$ values and calculate the transfer matrix M using Equation 38. The blue ellipses are output beam shape. By changing the $R_1 \sim R_4$ values and repeating the matrix calculation, we get reasonable ellipses whose major slopes agree with red reference slopes. In this way, we determine the coupling parameters at the exit of transport line. Because the 3−D spiral injection scheme requires a strongly coupled beam vertically and normally, the coupling parameters $R_1 \sim R_4$ are large compared to a typical beam line.

Lastly, we note that eight parameters (listed in Table 3) are required to determine the transfer matrix M. Therefore, we use eight rotated quadrupole magnets in the coupling section[2]. Once we decide the transfer matrix M, we can design real magnet components by use of **SAD** (Strategic Accelerator Design). Detailed discussions for practical design of beam transport line is found in [5].

[2]We may reduce the number of rotated quadrupole magnets to six, but we have decided to use 8 to allow greater flexibility

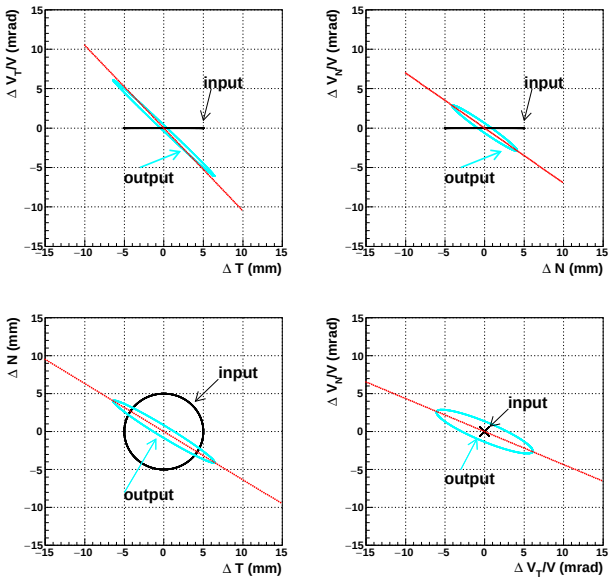

Figure 32: Explanation of an iterative calculation method using a simple model is shown. We set the input beam shape as a circle with radius 5 mm, and set the initial momentum spread to zero for both transverse and normal components. Black solid lines depict the input beam shape, and the red lines are the target slopes. By changing $R_1 \sim R_4$ values and repeating the matrix calculation, we get reasonable ellipses with major slopes that agree with the red target slopes. The blue ellipses are resulting output beam shape.

4. Weak focusing system and kicker

The muon storage ring for this experiment will be a precession field 3 Tesla solenoid with cylindrical iron poles and return yoke. The solenoid is being designed now in collaboration with a private company to a specification of $<$ 1 ppm variation of the field locally within the storage region. The storage region is defined on the mid-plane, with a radius of 33.3 ± 1.5 cm and height of ± 5 cm; a **weak focusing magnetic field** will be applied to keep vertical motion of the beam to within a few cm. In this section, we introduce two major topics.

- Weak focusing magnetic field in the storage volume
- Kicker from the injection area to the storage area

Detail discussion of weak focusing field index is given in [5].

4.1. Weak focusing magnetic field in the storage volume

To keep the beam within the storage region, we need to focus the beam horizontally and vertically. We will employ a **weak focusing magnetic field system** to the beam.

Ideal case. A weak focusing magnetic field in a cylindrical coordinate system is expressed as:

$$\begin{aligned} B_Z &= B_0 \left(1 - n\frac{\Delta R}{R}\right), \\ B_R &= -n\frac{Z}{R}B_0, \end{aligned} \tag{43}$$

here $B_0 = 3$ Tesla is the main solenoidal field at Z=0 cm. $R_0 = 33.3$ cm and $\Delta R = R - R_0$. The field index n is

$$n = -\frac{R_0}{B_0}\frac{\delta B_Z}{\delta R} \tag{44}$$

The focus condition is obtained when we set $0 < n < 1$. ($n < 1$; for radial focus. And $n > 0$; for vertical focus.)

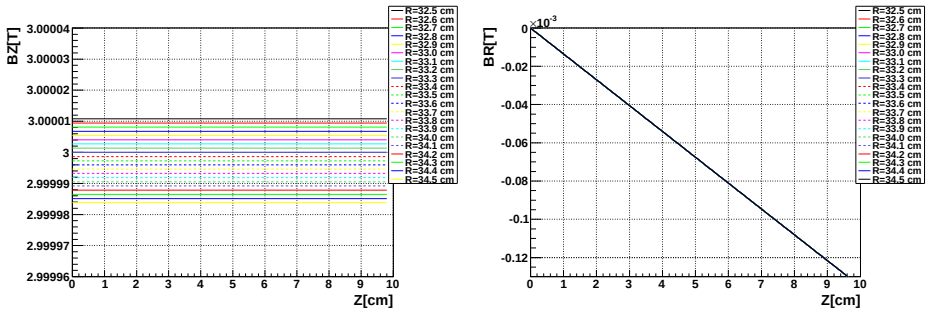

Figure 33: Example field of $n = 1.5 \times 10^{-4}$ case in Eq. 43.

Figure 33 depicts an example case of $n = 1.5 \times 10^{-4}$ in Eq. 43. Note that B_R does not change as a function of R, but changes vs. Z. B_Z, on the other hand, does change as a function of R, but does not change vs. Z.

We introduce horizontal (radial direction) and vertical (Z direction) transfer matrices for a single turn:

$$M_R = \begin{pmatrix} \cos\left(\frac{s}{R_0}\sqrt{1-n}\right) & \frac{R_0}{\sqrt{1-n}}\sin\left(\frac{s}{R_0}\sqrt{1-n}\right) \\ -\frac{\sqrt{1-n}}{R_0}\sin\left(\frac{s}{R_0}\sqrt{1-n}\right) & \cos\left(\frac{s}{R_0}\sqrt{1-n}\right) \end{pmatrix} \tag{45}$$

and

$$M_Z = \begin{pmatrix} \cos\left(\frac{s}{R_0}n\right) & \frac{R_0}{n}\sin\left(\frac{s}{R_0}n\right) \\ -\frac{n}{R_0}\sin\left(\frac{s}{R_0}n\right) & \cos\left(\frac{s}{R_0}n\right) \end{pmatrix} \tag{46}$$

here, s is the path length. $s = 2\pi R_0$ after single rotation in the horizontal plane.

Matrix at $s = 0 = 2\pi R_0$ is also expressed by use of twiss parameters $\beta(0), \alpha(s), \gamma(0)$ and phase advance $\mu(0)$ as follows:

$$M = \begin{pmatrix} \cos\mu(0) + \alpha(0)\sin\mu(0) & \beta(0)\sin\mu(0) \\ -\gamma(0)\sin\mu(0) & \cos\mu(0) - \alpha(0)\sin\mu(0) \end{pmatrix} \tag{47}$$

Set $n = 1.5 \times 10^{-4}$, and comparing Eq. 47 and Eq. 45 or Eq. 46, we obtain $\beta(0)$, $\alpha(0)$, $\gamma(0)$ and tune $\nu(0) = \mu(0)/2\pi$ for horizontal motion.

$$\begin{aligned} \beta_R(0) &= \frac{R_0}{\sqrt{1-n}} \cong 33.3\text{cm} \\ \alpha_R(0) &= 0 \\ \nu_R(0) &= \sqrt{1-n} \cong 0.999925 \end{aligned} \tag{48}$$

Similarly, parameters for vertical motion are

$$\begin{aligned} \beta_Z(0) &= \frac{R_0}{\sqrt{n}} \cong 26.94\text{m} \\ \alpha_Z(0) &= 0 \\ \nu_Z(0) &= \sqrt{n} \cong 1.2247 \times 10^{-2} \end{aligned} \tag{49}$$

Momentum dispersion is:

$$\begin{aligned} \eta(s) &= \frac{2R_0}{1-n} \cong 66.6\text{m} \\ \eta'(s) &= 0 \end{aligned} \tag{50}$$

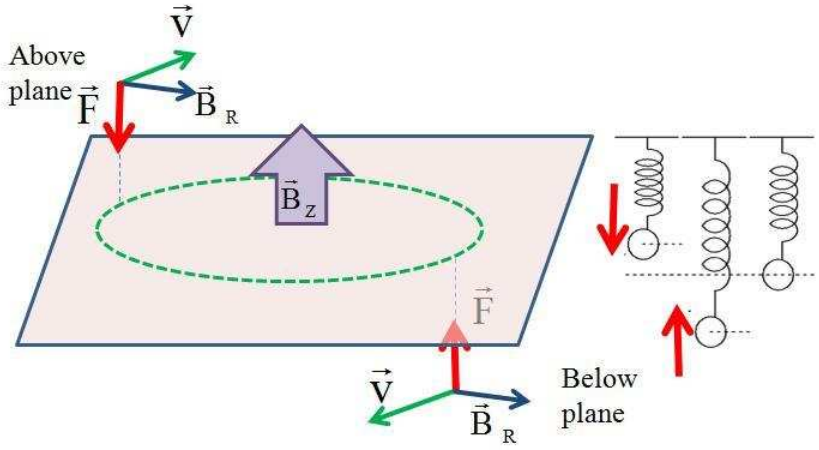

Figure 34: In the weak focusing volume, the muon is trapped in the potential. Its vertical beam motion is simple harmonic motion.

Figure 34 depicts the vertical motion in the weak focusing field. This is simple harmonic motion. The green dashed circle is the central orbit on the horizontal plane. If the muon is above (or below) the plane, the muon receives a downward(upward) force. One cycle of vertical simple harmonic motion takes 604.2 nsec for n=1.5×10^{-4}. This value is far away from the $g-2$ period 2.2 μsec.

Designed weak focusing field. Figure 35 depicts a realistic weak focus field designed by a private company H. We design the good field region to be between

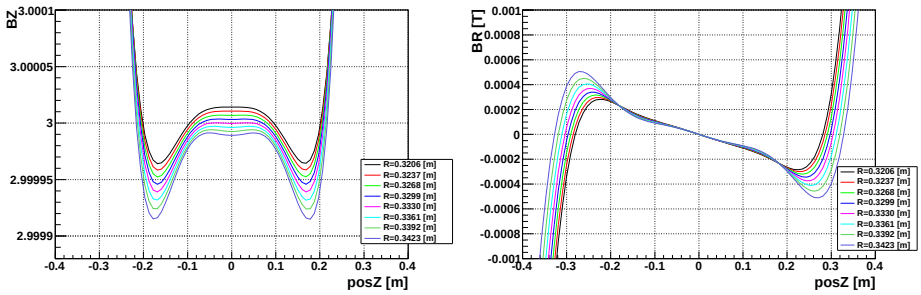

Figure 35: Realistic example field designed by Private company H.

$|z| < 10cm$ for stored beam. Because the B_R shape is good for $|z| < 20cm$, we consider this region to represent the weak focusing field.

Applying this field information, the vertical phase-space correlation in the storage area is estimated by Runge-Kutta integration. Results are shown in Fig. 36 as gray lines. Closed ellipses, which are between $|z| < 25cm$, correspond to trapping orbits. V_Z/V is the pitch angle of the muon. In the storage region, a pitch angle changes negative and positive alternately. We estimate the vertical tune from Fig. 36. The value is consistent with Eq. 49. The green arrow in Figure 36 depicts the action of a vertical kick from the injection volume to the storage volume. We are aiming to store the beam within $|z| < 10mm$. We will discuss the vertical kicker in section 4.2.

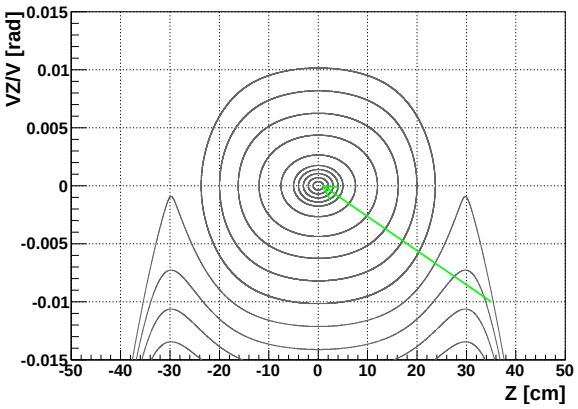

Figure 36: Phase-space correlation estimation with realistic weak field. Closed ellipses, which are in between $|z| < 25cm$, corresponds to trapping orbits. V_Z/V is the pitch angle of the muon. In the storage region, the pitch angle changes negative and positive alternately. The green arrow depicts the action of a vertical kick.

4.2. Vertical kicker

The role of the kicker is to kick the muon beam into the very center of the storage volume. The muon beam is guided down to $z \sim 35cm$ by the solenoidal fringe field only, reducing the pitch angle of the incoming beam to ten degrees. Then, the muon beam crosses the edge potential of the weak focusing field. In the weak focusing field, the muon beam motion becomes simple harmonic motion in vertical and the designed vertical amplitude is 10 mm.

We plan to apply the vertical kick for several tens of cyclotron periods. This allows us to set the peak kicker power lower, without strict jitter requirements. Yellow triangle in the center of in Figure 2 depicts an image of kicker action where the 3-D injected beam becomes almost a 2-D stored beam.

In this section we discuss the requirements for the kicker field, first. Secondly, we introduce the design of the Kicker system and a study using a test bench.

Requirement for kicker field. Pulsed axisymmetrically-excited field is required for the vertical kicker. For our case, the radial field component is important. Its time dependence is,

$$B_{kick}(t) = B_{peak} \cdot \sin\left(\frac{t}{2\pi T_{kick}}\right) \cdot \exp\left(-\frac{t}{\tau}\right), \tag{51}$$

with B_{peak} of order a few Gauss, and T_{kick} several hundred *nsec*.

We have tried calculations with Runge-Kutta integration for several types of kicker field, summarized in Table 4. In the second column in the table, sine type means that its time distribution is a single sine wave shape, and kick period is T_{kick}. Similarly, half-sine means that its time distribution is a half sine wave shape, and kick period is $T_{kick}/2$.

In this study, we set B_{peak} constant for simplicity. But we should consider spatial distribution of B_{peak} for a more realistic study.

Figure 37 depicts five types of kicker action with a single muon. A muon receives the kick force from the height z= $35cm$, then reduces its absolute pitch angle as the height goes zero. The path from the start to the end points are different between sine and half-sine types. Black and red lines corresponds to

type number	line color	shape	B_{kick} Gauss	T_{kick} nsec	τ nsec nsec	acceptable or not
1	black	sine	2	500	2000	◯
2	red	sine	1.7	530	∞	◯
3	green	half-sine	4	390	2000	×
4	blue	half sine	3	480	∞	×
5	orange	half-sine	2.2	655	∞	△

Table 4: Five types of kicker parameters.

a sine type kicker. The other three lines correspond to half-sine type kicker. Sine types pass through the horizontal mid-plane (z= 0), and reach z= −20 cm. Then they change the sign of pitch angle from negative to positive, and finally converge to the very center region. On the other hand, half-sine types do not go below the horizontal plane. They directly converge to the center region. This study shows us several possible types of vertical kicker configuration. However because of an electronics design limitation, we have learned that a field strength below 2 Gauss is a realistic number. Therefore, we decide that type-2 is a good candidate. The maximum value 2 Gauss is obtained from a study at the kicker test bench. We will discuss this topic in the next section .

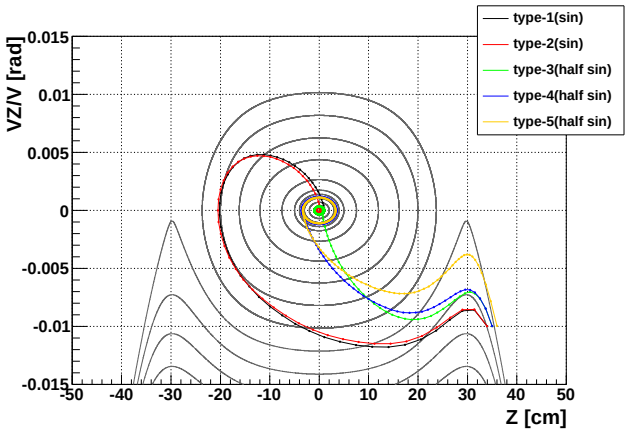

Figure 37: Five types of kicker action is shown.

Figure 38 depicts sample trajectories of kicker type-2. Figures 39 and 40 are magnified views of the end and start points of kick action. The red thick closed line in the right plot shows the envelope of the beam phase-space correlation around the vertical position z=35 cm. This line corresponds to the green line in Figure 20. If we could inject the beam inside of this red closed line, and apply a proper kick, the beam would be stored in the very center $|z| < 10$ mm. This is the goal of the beam injection.

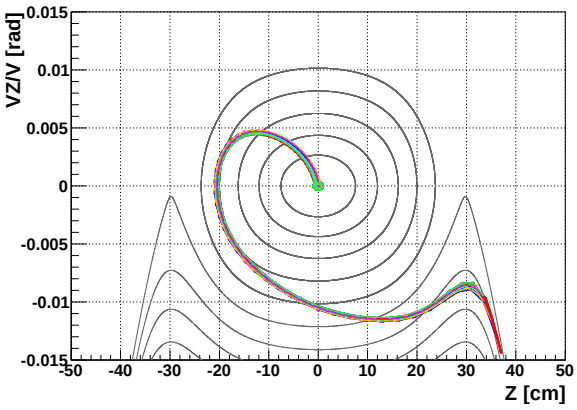

Figure 38: Sample trajectories of type-2 kicker.

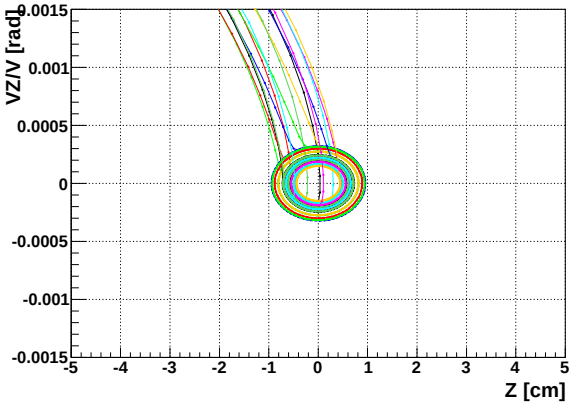

Figure 39: Magnified view of the end point of kicker action in Figure 38.

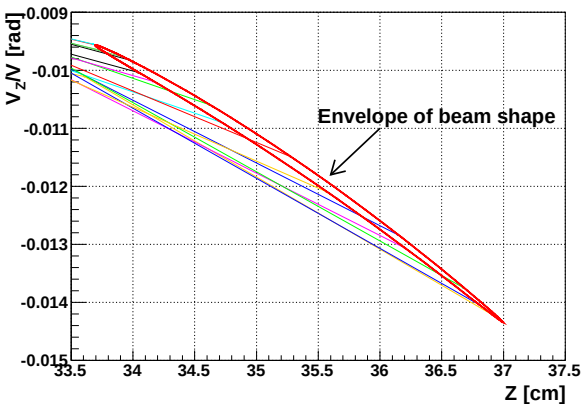

Figure 40: Magnified view of the start point of kicker action in Figure 38. The red envelope corresponds to the green line in Figure 20.

Real design of the kicker. Figure 41 depicts the kicker coils set-up in the storage ring: An anti-Helmholtz type coil system (which does not satisfy the exact Helmholtz condition), shown in red, has four loops. Pairs of coils above and below the horizontal plane have different radii and are separated 6 cm horizontally. The upper and lower coils are separated by 35 cm. The kicker coils do not interfere with the storage nor detector volumes. (There is a small interference for positrons from decaying muons at one position of azimuth.)

The current direction of the upper pair of coils is clockwise. The current in the lower pair of coils is counterclockwise. Such a coil system generates mainly a radial field around the region of $|z| < 35$ cm. This radial field is cylindrically symmetric and applies a vertical kick to the muon beam.

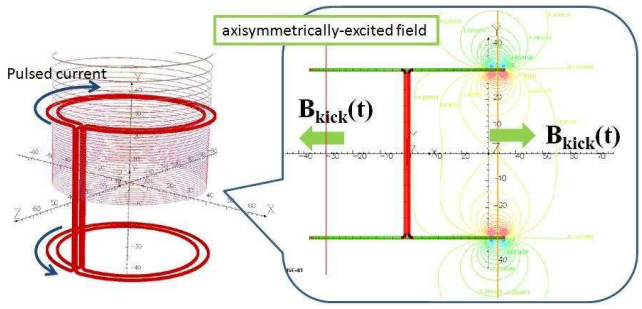

Figure 41: Image of kicker coils. The inner and outer radii are 30 cm and 36 cm, respectively and the upper and lower coils are located at $z = \pm 35$ cm. The current is opposite between the upper and lower coils. This coil system generates mainly a radial field around the region of $|z| < 35$ cm.

4.3. Potential issues on the weak field and the kicker system

Horizontal error field estimation. The horizontal transfer matrix shown in Eq. 45 is rewritten as

$$M_R \cong \begin{pmatrix} \cos\frac{s}{R_0} & R_0 \sin\frac{s}{R_0} \\ -\frac{1}{R_0}\sin\frac{s}{R_0} & \cos\frac{s}{R_0} \end{pmatrix} \tag{52}$$

where we use $n \cong 0$. We assume the presence of a horizontal error field in a certain small region δl along the orbit. This error field gives a horizontal kick

to the beam. As shown in the left side of Fig. 42, the horizontal momentum direction is changed for every turn by horizontal kicks as:

$$\theta_{kick} \equiv \frac{\Delta B_Z}{B}\frac{\delta l}{R_0}. \tag{53}$$

Since the horizontal tune$\cong 1$, the beam is kicked every turn in the same region. In this case, displacement from the ideal orbit becomes large at two points: $\phi = \pi/2$ and $\phi = 3\pi/4$ as shown in the right side of Fig. 42.

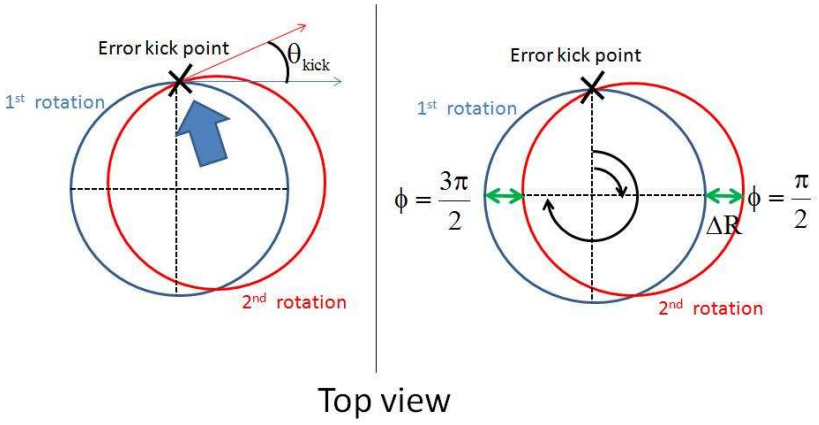

Figure 42: Left: horizontal momentum direction is changed for every turn by horizontal kicks. Right: displacement from the ideal orbit becomes large at two points:$\phi = \pi/2$ and $\phi = 3\pi/4$.

The displacement ΔR is,

$$\Delta R = R_0 \Delta\theta_{kick} \tag{54}$$

for a single turn. To control the displacement Δ_{kick} to within 5 mm for up to $m = 5000$ turns, $mR_0\theta_R \leq 5$ mm, and the kick angle for each turn should be $\theta_{kick} \leq 3 \times 10^{-5}$. Therefore, we have

$$\frac{\Delta B_Z}{B}\frac{\delta l}{R_0} \leq 3 \times 10^{-5}. \tag{55}$$

Finally we get the error field requirement for B_Z variation in horizontal plane

$$\frac{\Delta B_Z}{B} \leq 1 \times 10^{-6} \text{ for } \delta l = 10\text{cm}. \tag{56}$$

Vertical error field estimation. The vertical transfer matrix shown in Eq. 46 is rewritten as

$$M_Z = \begin{pmatrix} 1 & s \\ -\frac{ns}{{R_0}^2} & 1 \end{pmatrix} \tag{57}$$

where we use $n \cong 0$. This matrix is approximately a drift matrix in free space. The error kick for a single turn for the vertical direction is

$$\theta_{kick} \equiv \frac{\Delta B_R}{B} \frac{\delta l}{R_0}. \tag{58}$$

The vertical displacement after mth turns becomes

$$\Delta Z \cong 2\pi R_0 \theta_{kick} \frac{m-2}{2}. \tag{59}$$

Since the vertical tune is 8.9×10^{-3}, the beam turns 112 times horizontally during one cycle of vertical beam motion. That is, the vertical direction of beam motion flips every 56 turns as shown in Fig. 43.

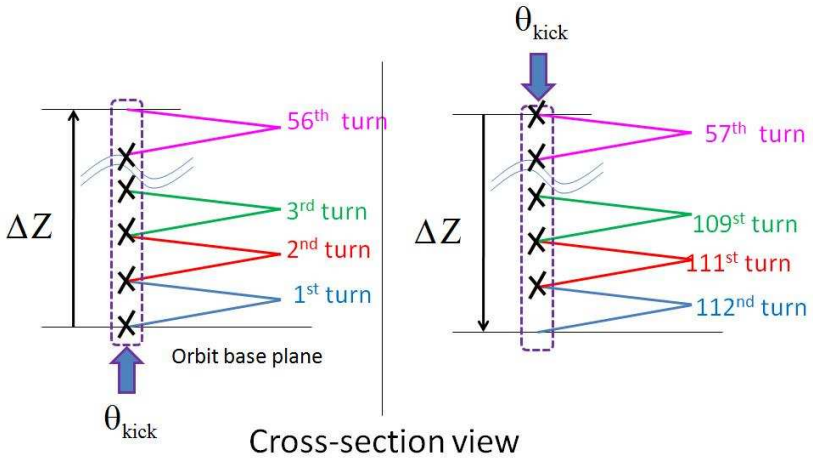

Figure 43: Vertical direction of beam motion flipped at every 56 turns due to the vertical tune of 8.9×10^{-3}. The beam turns 112 times horizontally during one cycle of vertical beam motion.

500

To control displacement Δ_{kick} within 5 mm up to $m = 56$ turns, $mR_0\theta_{kick} \leq$ 5 mm, the kick angle for each turn should be $\theta_{kick} \leq 1.52 \times 10^{-6}$. Therefore,

we have

$$\frac{\Delta B_R}{B}\frac{\delta l}{R_0} \leq 1.52 \times 10^{-6}. \tag{60}$$

Finally we get

$$\frac{\Delta B_R}{B} \leq 4.8 \times 10^{-6} \text{ for } \delta l = 10\text{cm}. \tag{61}$$

For both horizontal and vertical, the weak focusing field should be controlled to a 1 ppm level of the main field B=3T.

the Kicker system. Two potential issues for the kicker are eddy currents and induced voltage in a quench.

Eddy currents generated in the cryostat wall cause an *error field* that needs to be considered carefully. We estimated the field from an eddy current on the Cryostat wall at the radius=60cm by OPERA simulation.

We tried two types of materials for the cryostat wall; one is SUS304(stainless iron) and the other is aluminum. Figure 44 displays the total eddy current in the cryostat wall as a function of time. Eddy currents from both materials are nearly identical and cannot be separated on the plot.

The profile of the eddy current is similar to that of the kicker current. and does not stay in the wall more than 10 ns after the kicker pulse. Figure 45 displays the current density profile at t=100 ns. The strength of field changes as a function of time, while the density profile on the wall surface does not change much and the dominant component of the current direction is parallel to the kicker coils.

By use of this profile, we estimate the *residual* field strength from the kicker around the region of the muon orbit as displayed in Fig. 47. The horizontal axis corresponds to the vertical position. The plot covers the $|z| < 10$ cm region where the muon beam stays in the first few hundred nsec. Note that the residual field for the solenoid axis and radial components ΔB_R and ΔB_z are negligible compared to the main field ($B_z = 3$ Tesla) from the main coils at the level of 0.1 ppb at t$\geq$ 160 ns. From this study, we conclude that the field from eddy current on the cryostat wall goes off t$\geq$ 160 ns at the level of 0.1 ppb.

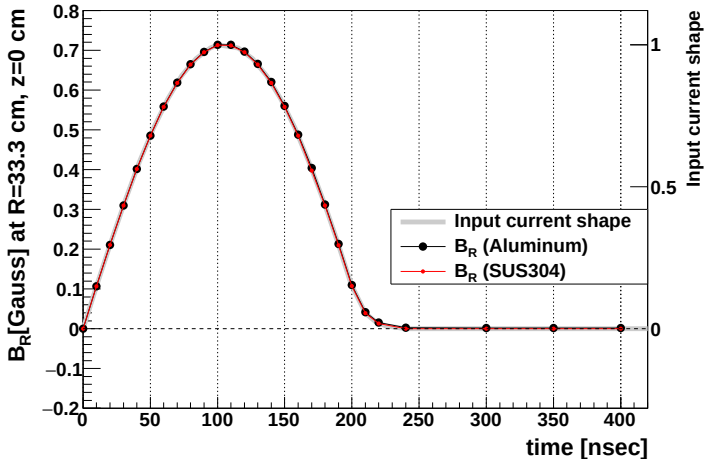

Figure 44: Calculation of total eddy current in the wall as a function of time. Time=0 ns is the rising edge of the kicker current. Eddy currents from both materials are very similar. The profile of the eddy current is similar to that of the kicker current (T_{kick} = 150 ns, and does not stay in the wall.

As for the quench effect on the kicker system, it turns out that this effect is quite small and negligible, because the decay time from the maximum field strength B=3 Tesla is the order of a few seconds. For example, in the case of decay time Δt = 1 sec, the dielectric voltage V per kicker coil (radius=0.5m, area S=0.785 m^2) from the quench is

$$V = -\frac{\Delta\Phi}{\Delta t} = 2.5 \text{ (V)}. \tag{62}$$

Here,

$$\Delta\Phi = B \cdot S = 3 \cdot 0.785 \text{ (Tesla} \cdot \text{m}^2\text{)}. \tag{63}$$

The induced voltage from the quench effect can be easily consumed by the normal resistors in the power supply circuit.

Other major issues for the kicker are the following:

- Kicker field flatness as function of radial position,
- Residual voltage in the circuit may cause an electric field in the space,

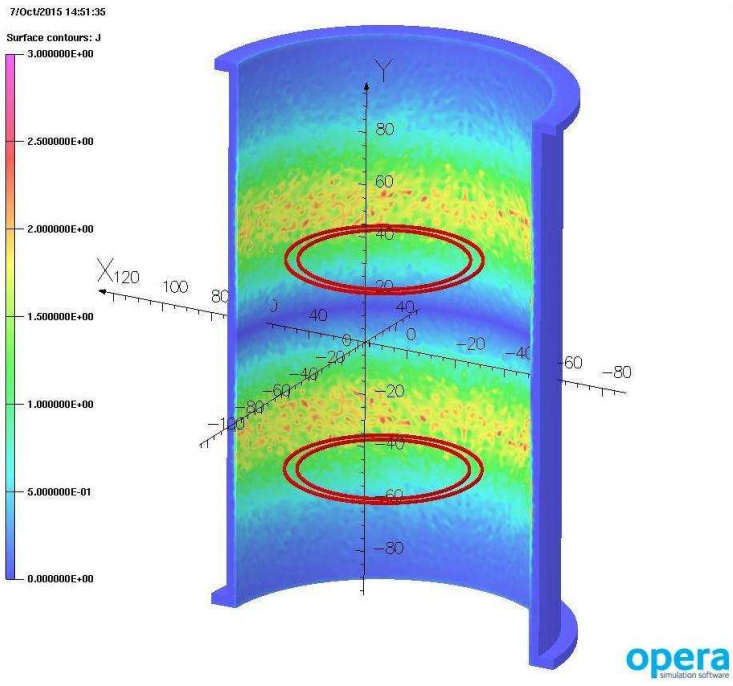

Figure 45: Eddy current density on the SUS316 surface at radius=60 cm at time t=100 ns. The left side graph legend colors shows current densities from 0 to 3 A/cm^2. Yellow and red regions correspond to $\sim$ 2 A/cm^2. The two pairs of kicker coils are shown in red.

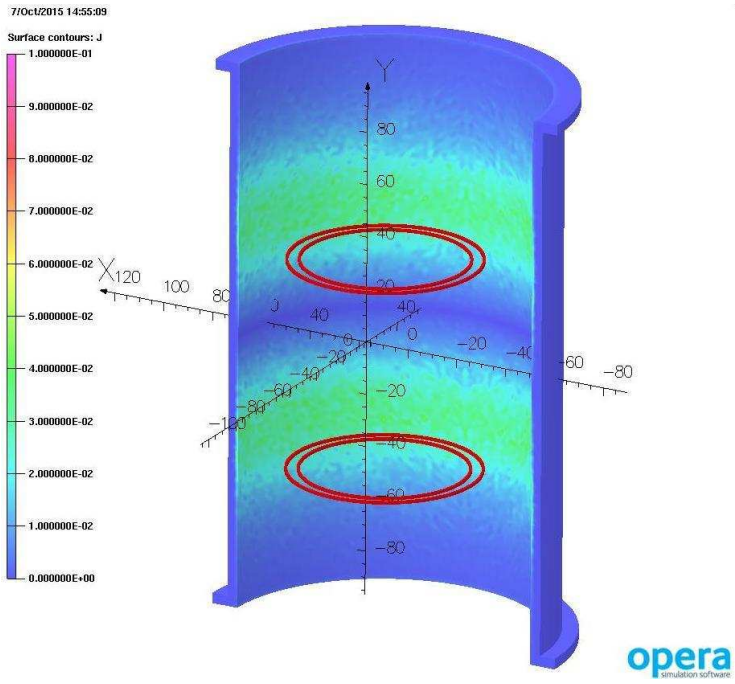

Figure 46: Eddy current density on the SUS316 surface at radius=60 cm at time t=220 ns. The left side graph legend colors shows current densities from 0 to 0.1 A/cm^2. Green region corresponds to 0.04 A/cm^2. The two pairs of kicker coils are shown in red.

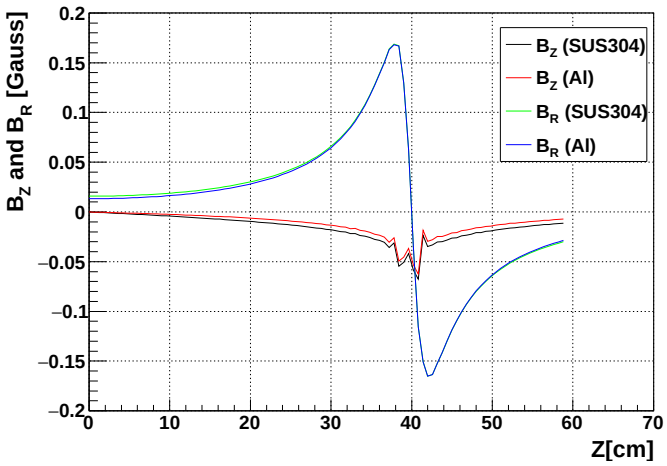

Figure 47: Residual magnetic field strength (Tesla) from the eddy current as a function of vertical position (solenoid axis direction). The black solid line corresponds to the field component along the solenoid axis ΔB_z. The red dotted line corresponds to radial field ΔB_R. The horizontal axis corresponds to vertical position. This plot covers the $|z| < 10$ cm region where the muon beam stays in the first few hundred nsec. Note that these ΔB_R and ΔB_z are the residual field from eddy current. We have $B_z = 3$ Tesla from the main coils. Therefore the residual field from eddy current goes off t$\geq$ 160 ns at the level of 0.1 ppb.

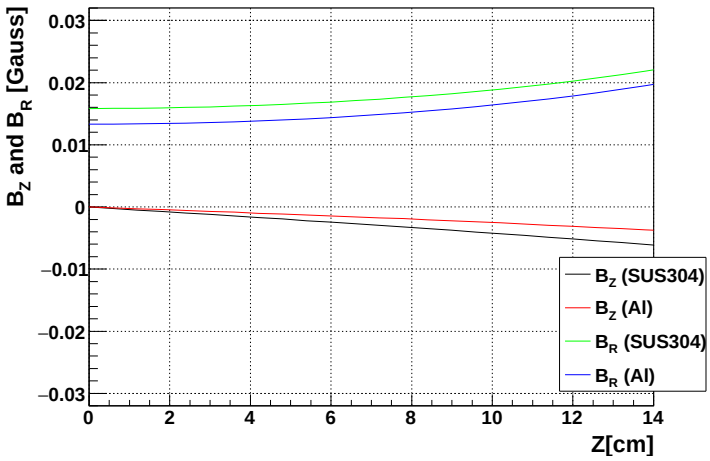

Figure 48: Residual magnetic field strength (Tesla) from the eddy current as a function of vertical position (solenoid axis direction). The black solid line corresponds to the field component along the solenoid axis ΔB_z. The red dotted line corresponds to radial field ΔB_R. The horizontal axis corresponds to vertical position. This plot covers the $|z| < 10$ cm region where the muon beam stays in the first few hundred nsec. Note that these ΔB_R and ΔB_z are the residual field from eddy current. We have $B_z = 3$ Tesla from the main coils. Therefore the residual field from eddy current goes off t$\geq$ 160 ns at the level of 0.1 ppb.

We are determining to the best configuration for the coils and expect to achieve sufficient field flatness.

5. Further studies for the higher injection efficiency

We discuss how to estimate injection efficiency and what items are needed as further studies. Injection efficiency is estimated by counting how much muons, which are in the given phase-space at the exit of the LINAC (or the entrance ob the transport line), can be injected in to a required phase-space area which satisfies criteria at the kick point ($z \sim 35$ cm) shown in Figure 40. (See discussion in Section 3) Note that these injection efficiencies can be changed depend on the kicker parameters. Actually, we continue to make efforts to broaden the areal size of Figure 40 now.

In the current condition, we estimate injection efficiencies at several initial beam conditions at the entrance of the transport line. Table 5 shows the summarize numbers. The third column shows the numbers of successfully injected muons divided by total injection.

At first we tried cases of momentum dispersion $\Delta p/p$ are zero. We have two sets of initial $\beta_{N,T} = 10$ or $\beta_{N,T} = 20$ [3]. We also have two more subsets: with or without horizontal and vertical coupling cases. In the same way, we tried momentum dispersion of $\Delta p/p \leq 0.05\%$ cases, $\Delta p/p \leq 0.1\%$ cases and $\Delta p/p \leq 1\%$ cases.

From this study, we learned:

- the beam momentum dispersion within $\pm 0.05\%$ is acceptable,
- Initial twiss parameter $beta = 20$ is good for phase-space matching.
- Thinner beam shape is favored
- Horizontal-vertical coupling is important (if we do not apply proper coupling, efficiency decrease down to factor 2).

[3] $\beta_{N,T}$ is twiss parameter introduced in Section 3.1.

Δp/p	$\beta_{N,T}$	coupling	good/tot	ratio	acceptable or not
0	10	yes	340/400	85%	◯
		no	247/400		△
	20	yes	368/400	92%	◯
		no	246/400		△
$\leq 0.5\%$	10	yes	52/400		×
		no	55/400		×
	20	yes	52/400		×
		no	52/400		×
$\leq 0.1\%$	10	yes	233/400		△
		no	170/400		×
	20	yes	243/400		△
		no	199/400		△
$\leq 0.05\%$	10	yes	304/400	76%	◯
		no	197/400		×
	20	yes	331/400	83%	◯
		no	236/400		△

Table 5: Comparison among two types initial twiss parameter β and with/without coupling. Momentum dispersion of the muon beam $\Delta p/p \leq 0.05\%$ is acceptable. $\beta_{N,T} = 20$ is better than $\beta_{N,T} = 10$ case. Without rotation matrix, injection efficiency decreases by factor two.

6. Conclusion

We described a new conceptual design of three dimensional spiral injection scheme, which is an unprecedented injection technology in the world. In order to achieve 1 ppm level of field uniformity in the beam storage volume, we utilize 3 T MRI-type solenoid magnet. Diameter of the storage ring is only 0.66 m with 300 MeV/c muon beam. Conventional injection scheme is not applicable to such a compact ring, but the newly developed scheme does work.

Starting from a single muon kinetics, we discussed an acceptance of beam phase-space at the entrance point of the storage magnet as well as strong coupling between horizontal and vertical beam phase-space. We also described a transfer matrix to create such a strong coupled beam. At the exit of the LINAC, the beam is supposed to be no coupling. Therefore we need to apply appropriate coupling to the muon beam at the beam transport line between the exit of LINAC to the entrance of the storage magnet. Weak focusing magnetic field and the vertical kicker system are described. Field index of Weak focusing field is determined to avoid coincidence with $g-2$ frequency. But we still need for further studies to find the best parameters of field strength and time structure of the kicker.

Demonstrate a feasibility of the newly developed injection scheme is important. Test experiment is now running. Utilizing 100 keV electron beam, we try to inject the electron beam into the test solenoid magnet (100 Gauss). We expect to have many feed backs which should be reflected on the detailed engineering design from the test experiment.

References

[1] G. W. Bennett *et al.* [Muon ($g2$) Collaboration]. Final report of the muon e821 anomalous magnetic moment measurement at bnl. *Phys. Rev. D*, 73(072003), 2006.

[2] G. W. Bennett *et al.* [Muon (g 2) Collaboration]. An improved limit on the muon electric dipole moment. *Phys. Rev. D*, 80(052008), 2009.

[3]

[4]

[5] Technical design report for the measurement of the muon anomalous magnetic moment g–2 and electric dipole moment at j-parc. *unpublished*.

[6] A. Yamamoto *et al.* The superconducting inflector for the bnl g-2 experiment. *Nucl. Inst. Method.*, A 491:23–40, 2002.

[7] K. Shibata M. Abe. Consideration o current coil block placement with good homogeneity for mri magnets using truncated svd. *IEEE Trans. Magn.*, 49(6):2873–2880, 2013.

[8] K. Shibata M. Abe. Coil block designs with good homogeneity for mri magnets based on svd eigenmode strengths. *IEEE Trans. Magn.*, 51(10):7002713, 2015.